

1 **FILE 1: TITLE PAGE**

2  
3  
4 **Time-lapse photogrammetry reveals hydrological controls of fine-**  
5 **scale High-Arctic glacier surface roughness evolution**

6  
7 Tristram D L Irvine-Fynn<sup>1\*</sup>, Tom O Holt<sup>1</sup>, Timothy D James<sup>2</sup>, Mark W  
8 Smith<sup>3</sup>, Nick Rutter<sup>4</sup>, Philip R Porter<sup>5</sup>, Andrew J Hodson<sup>6,7</sup>.

9  
10 1. Department of Geography and Earth Sciences, Aberystwyth University,  
11 Aberystwyth, UK.

12 2. Department of Geography and Planning, Queen's University, Kingston,  
13 Ontario, Canada.

14 3. School of Geography, University of Leeds, Leeds, UK.

15 4. Department of Geography and Environmental Sciences, Northumbria  
16 University, Newcastle, UK.

17 5. School of Life and Medical Sciences, University of Hertfordshire,  
18 Hatfield, UK.

19 6. University Centre in Svalbard (UNIS), Longyearbyen, Svalbard,  
20 Norway.

21 7. Western Norway University of Applied Sciences, Sogndal, Norway

22  
23  
24 **CONTACT DETAILS OF THE CORRESPONDING AUTHOR**

25  
26 \*Email: tdi@aber.ac.uk

27  
28 **ORCID IDs:**

29  
30 TDL Irvine-Fynn: 0000-0003-3157-6646

31 TO Holt: 0000-0001-8361-0688

32 TD James: 0000-0003-4082-7822

33 MW Smith: 0000-0003-4361-9527

34 N Rutter: 0000-0002-5008-3575

35 PR Porter: 0000-0001-5618-9189

36 AJ Hodson: 0000-0002-1255-7987

37  
38 **ACKNOWLEDGEMENTS**

39  
40 TDLI-F acknowledges The Leverhulme Trust (Grant: RF-2018-584/4). The  
41 University Centre in Svalbard (UNIS) is thanked for the logistical support  
42 of fieldwork. AJH acknowledges The Royal Geographical Society - Peter  
43 Fleming Award, a National Geographic Research and Exploration grant  
44 and Store Norske Spitsbergen Kulkompani AS for the help in establishing  
45 the monitoring at Foxfonna. Support from TerraDat with Topcon's Image  
46 Master Pro was gratefully received by TDJ. Pete Bunting is thanked for  
47 help adapting the energy balance model code, and Morgan Jones and

48 Hywel Griffiths proof-read versions of the manuscript. TDLI-F thanks Jim  
49 Chandler for a late-night conversation at an 'Arolla project reunion' well  
50 over a decade ago suggesting that 'if there was enough texture maybe  
51 one commercial grade camera and some photogrammetry might reveal  
52 the topographic dynamics of an ice surface'. How the field developed!

53

#### 54 **AUTHOR CONTRIBUTIONS**

55

56 Conceptualization – TDLI-F; Funding acquisition – TDLI-F, AJH;  
57 Methodology TDLI-F, TDJ; Investigation – TDLI-F, TDJ, TOH, MWS, NR;  
58 Resources – TDLI-F, AJH, PRP, MWS, NR; Writing draft – TDLI-F; Editing  
59 and revising – all authors.

60

#### 61 **DATA AVAILABILITY STATEMENT**

62

63 The datasets generated during and/or analysed in this study are available  
64 in the Zenodo repository (<https://doi.org/10.5281/zenodo.5784564>). The  
65 base energy balance model, in Python, is available at:  
66 <https://github.com/atedstone/ebmodel>.

Authors Copy  
ESP&L Spec Issue  
Accepted 30-12-2021

1  
1 **FILE 2: MAIN DOCUMENT**

2  
3 **Time-lapse photogrammetry reveals hydrological controls of fine-**  
4 **scale High-Arctic glacier surface roughness evolution**

5  
6 **Abstract**

7  
8 In a warming Arctic, as glacier snowlines rise, short- to medium-term  
9 increases in seasonal bare-ice extent are forecast for the next few  
10 decades. These changes will enhance the importance of turbulent energy  
11 fluxes for surface ablation and glacier mass balance. Turbulent energy  
12 exchanges at the ice surface are conditioned by its topography, or  
13 roughness, which has been hypothesised to be controlled by supraglacial  
14 hydrology at the glacier scale. However, current understanding of the  
15 dynamics in surface topography, and the role of drainage development,  
16 remains incomplete, particularly for the transition between seasonal snow  
17 cover and well-developed, weathered bare-ice. Using time-lapse  
18 photogrammetry, we report a daily timeseries of fine (millimetre)-scale  
19 supraglacial topography at a 2 m<sup>2</sup> plot on the Lower Foxfonna glacier,  
20 Svalbard, over two 9-day periods in 2011. We show traditional kernel-  
21 based morphometric descriptions of roughness were ineffective in  
22 describing temporal change, but indicated fine-scale albedo feedbacks at  
23 depths of ~60 mm contributed to conditioning surface topography. We  
24 found profile-based and two-dimensional estimates of roughness revealed  
25 temporal change, and the aerodynamic roughness parameter,  $z_0$ , showed  
26 a 22-32% decrease from ~1 mm following the exposure of bare-ice, and  
27 a subsequent 72-77% increase. Using geostatistical techniques, we  
28 identified 'hole effect' properties in the surface semivariograms, and  
29 demonstrated that hydrological drivers control the plot-scale topography:  
30 degradation of superimposed ice reduces roughness while the inception of  
31 braided rills initiates a subsequent development and amplification of  
32 topography. Our study presents an analytical framework for future studies  
33 that interrogate the coupling between ice surface roughness and hydro-  
34 meteorological variables and seek to improve parameterisations of  
35 topographically evolving bare-ice areas.

36  
37 **Keywords:**

38 Glacier surface, roughness, photogrammetry, hydrology, semivariance

## 39 **1. INTRODUCTION**

40 Across the Arctic region, glacier equilibrium lines are rising (Curley *et al.*,  
41 2021; Ryan *et al.*, 2019; Noel *et al.*, 2019; 2020). Consequently, over the  
42 coming few decades, the spatial extent of bare-ice during the ablation  
43 season is expected to increase as the glaciers thin and recede (Huss and  
44 Hock, 2015). The rate of melting in these bare-ice areas is controlled by  
45 the radiative and turbulent energy fluxes, which are regulated,  
46 respectively, by the ice surface's albedo and topography (Hock, 2005). In  
47 many continental glacierized locations radiative fluxes dominate the  
48 surface energy balance ( $\sim 77\%$ ); however, in climate regimes where cloud  
49 cover is commonplace, the turbulent fluxes become more substantial  
50 contributors, accounting for up to 80% of the energy available for ablation  
51 (Willis *et al.*, 2002). Phases of elevated turbulent energy fluxes are  
52 commonly associated with synoptic 'melt events', which are often coupled  
53 with rainfall, or occur during the ablation-to-accumulation season  
54 transition period (e.g., Hay and Fitzharris, 1988; Gillett and Cullen, 2011;  
55 Giesen *et al.*, 2014; Doyle *et al.*, 2015; Fausto *et al.*, 2016). With  
56 observations and forecasts of amplified warming in the Arctic (e.g.,  
57 Overland *et al.*, 2019), increasing synoptic rainfall events (Bintanja, 2018,  
58 Bintanja *et al.*, 2020), and an underestimation of cloud feedbacks (e.g.,  
59 Middlemas *et al.*, 2020), future projections of the region's glacier mass  
60 balance demand improved spatial and temporal parameterizations of ice  
61 topography and turbulent energy fluxes.

62 Melting bare-ice glacier topography is complex and dynamic. This  
63 variability, at the local scale, is driven by spatially differing ablation  
64 caused by: crystal anisotropy (e.g., Greuell and de Ruyter de Wildt,  
65 1999); emergent ice structures (e.g., Hambrey and Lawson, 2000;  
66 Hudleston, 2015; Jennings and Hambrey, 2021); non-stationary  
67 impurities (including dust and cryoconite: e.g., Gribbon, 1979; Bøggild *et al.*,  
68 2010; Irvine-Fynn *et al.*, 2011; Neild *et al.*, 2013; Takeuchi *et al.*,  
69 2018); and incipient surface hydrology and 'micro-channels' (Mantelli *et al.*,  
70 2015; Rippin *et al.*, 2015; Bash & Moorman, 2020). However,  
71 synoptic influences further complicate the evolution of topography: for  
72 example, surface morphology can be reduced or eliminated during periods  
73 of enhanced turbulent energy fluxes and/or rainfall-driven conductive and  
74 latent heat exchanges (Muller and Keeler, 1969; Takeuchi *et al.*, 2018;  
75 Liu *et al.*, 2020). Such close coupling between dynamic glacier surface  
76 characteristics and hydro-meteorology offers an explanation for the  
77 contrasting reports of spatial and temporal trends in topographic  
78 variability, with examples of systematic evolution (e.g., Herzfeld *et al.*,  
79 2003; Smeets and van den Broeke, 2008; Guo *et al.*, 2011; Lui *et al.*,

80 2020) countered by descriptions of incoherent change (e.g., Brock *et al.*,  
81 2006; Guo *et al.*, 2018). Reconciling these contrary perspectives, Smith  
82 *et al.* (2020) suggested that, at the deci- to deca-metre patch- or plot-  
83 scale, the temporal change in bare-ice surface topography is unordered,  
84 yet is organized and predictable at larger (glacier) scales, primarily owing  
85 to the progressive evolution of the supraglacial hydrological system.

86 Surface topography is commonly described by its texture or roughness,  
87 and of the many representations or metrics (Smith, 2014), the  
88 aerodynamic roughness length ( $z_0$ ) is commonly used to estimate the  
89 turbulent energy flux in numerical models of glacier ice melt (Hock,  
90 2005). Defined as the boundary layer height above the glacier surface at  
91 which wind velocity reduces to zero,  $z_0$  typically lies at the millimetre-  
92 scale over ablating bare-ice, but can vary over several orders of  
93 magnitude (Brock *et al.*, 2006, and references therein). Because turbulent  
94 energy fluxes are proportional to the square of the natural logarithm of  
95  $z_0$ , an increase in  $z_0$  from 2.2 to 5.5 mm can increase turbulent energy  
96 available for ice melt by 20% (Brock *et al.*, 2006). Yet, despite the recent  
97 increase in studies reporting bare-ice  $z_0$  (e.g., Smeets *et al.*, 1999; Rees  
98 and Arnold, 2006; Brock *et al.*, 2006; Smeets and van den Broeke, 2008;  
99 Guo *et al.*, 2011; Irvine-Fynn *et al.*, 2014a; Smith *et al.*, 2016; Guo *et*  
100 *al.*, 2018; Fitzpatrick *et al.*, 2019; Chambers *et al.*, 2019, 2021), the  
101 understanding of how glacier surface topography and  $z_0$  varies over space  
102 and time, at a range of scales, remains incomplete (e.g., Smith *et al.*,  
103 2020; Lui *et al.*, 2020). This is particularly the case for the trajectory of  
104 bare-ice as it transitions from superimposed ice with discrete residual  
105 snow patches to a mature surface topography defined by hydrology.

106 The relative paucity of quantifications of heterogenous, emergent bare-ice  
107 glacier surface roughness presents a persistent research challenge.  
108 Fitzpatrick *et al.* (2019) concluded that topographic representations at  $\sim 1$   
109 m horizontal resolution are required to define bare-ice roughness  
110 features,  $z_0$ , and, by inference, surface processes. Such a fine-scale lies  
111 below the resolution of many satellite-retrieved products used to monitor  
112 or represent glacier surface characteristics (Chambers *et al.*, 2021).  
113 Consequently, many numerical melt models use either time-constant  
114 values based on published estimates or tune the  $z_0$  roughness value to fit  
115 observed ablation or runoff observations (e.g., Arnold *et al.*, 2006; Giesen  
116 *et al.*, 2014; Fausto *et al.*, 2016; Østby *et al.*, 2017). These simplifications  
117 fail to reproduce the turbulent energy fluxes in a realistic manner (Hock,  
118 2005), and prompt the continued desire for refinement of current  
119 parameterisations of  $z_0$  in glacier and ice sheet surface energy balance  
120 models (e.g., van den Broeke *et al.*, 2017).

121 The spatial and temporal roughness patterns at metre to sub-metre  
122 scales can be informative not only for  $z_0$  but of dynamical processes,  
123 interactions, and feedbacks at the surface (Herzfeld *et al.*, 2000).  
124 However, these insightful length-scales correspond to those of  
125 supraglacial rills and streams and their spacing, cryoconite holes, foliation  
126 and other ice structure, and, importantly, to the scale-dependency of ice  
127 surface roughness between length-scales of 0.1 to  $\sim 2$  m (Rees and  
128 Arnold, 2006). Nonetheless, roughness variability at finer scales is  
129 essential to inform the response of, and uncertainties in data retrieved  
130 from assorted satellite platforms (Rees and Arnold, 2006; Fitzpatrick *et*  
131 *al.*, 2019; van Tiggelen *et al.*, 2021). Yet, despite such critical questions,  
132 assessments of bare-ice topographic dynamics, and their drivers, at high  
133 resolution remain lacking.

134 The capability of time-lapse imaging and modern photogrammetric  
135 methods to reveal fine-scale ice surface topographic change is evident in  
136 recent glaciological investigations (e.g., Rippin *et al.*, 2015; Ryan *et al.*,  
137 2015; Rossini *et al.*, 2018; Moorman and Bash, 2018), and exemplified by  
138 retrievals of fine-scale bare-ice topography (e.g., Irvine-Fynn *et al.*,  
139 2014a; Smith *et al.*, 2016; Smith *et al.*, 2020; Lui *et al.*, 2020). However,  
140 there remain relatively few studies that identify or verify processes  
141 defining surface roughness and seek to improve the parameterisation of  
142  $z_0$ . Here, we contribute to this research gap by presenting a novel, low-  
143 cost framework involving time-lapse photogrammetry to interrogate a  
144 fine-scale surface microtopography time-series, and explore the role of  
145 hydrology in conditioning glacier surface roughness at a High-Arctic site  
146 over two 9-day periods in 2011.

## 147 **2. FIELD SITE AND METHODS**

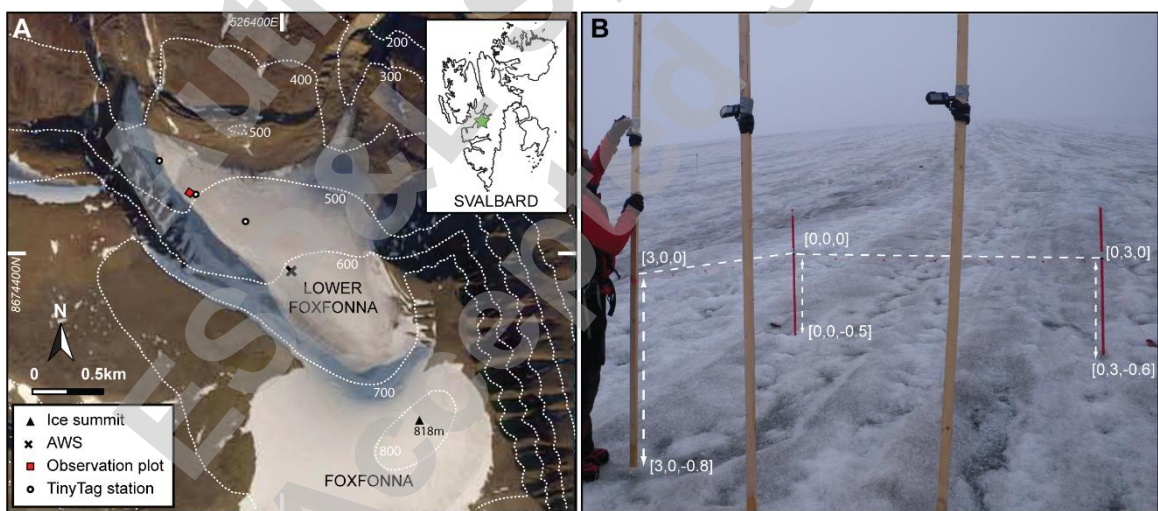
148 Svalbard harbours  $\sim 5\%$  of Earth's glacier ice volume outside Greenland or  
149 Antarctica (Martin-Espanol *et al.*, 2017), and is getting warmer and wetter  
150 (Hansen-Bauer *et al.*, 2020), with rising seasonal snow-lines and  
151 increased bare glacier ice extents during summer months (Noel *et al.*,  
152 2020). In this climate-sensitive, glacierized locality, at Foxfonna (78.1°N,  
153 16.2°E) we generated fine (millimetre) -scale surface elevation models for  
154 a bare-ice plot to explore the temporal dynamism of roughness, which  
155 defines the turbulent energy exchanges at the glacier surface and holds  
156 relevance for summer mass balance across the changing Arctic region.

### 157 **2.1 Foxfonna**

158 Foxfonna is a small, high-elevation ice cap complex, which extends over  
159  $< 10$  km<sup>2</sup> to  $\sim 820$  m a.s.l., with two principal outlet glaciers discharging

160 ice to lower elevations: the increasingly disconnected Rieperbreen to the  
 161 west, and Lower Foxfonna to the north (Christiansen *et al.*, 2005; Rutter  
 162 *et al.*, 2011). Lower Foxfonna is assumed to be cold-based, despite ice  
 163 thicknesses of up to 125 m (Liestøl, 1974; Christiansen *et al.*, 2005), with  
 164 surface elevations ranging from ~380 to 700 m a.s.l. where the glacier is  
 165 fed by an icefall descending from the ice cap (Figure 1A). The Lower  
 166 Foxfonna glacier flows north-west towards a large boulder moraine ridge,  
 167 bifurcating into two narrow tongues that extend to the north and north-  
 168 west, respectively.

169 During the melt season in 2011, we instrumented the larger, ~1.3 km<sup>2</sup>  
 170 north-western portion of the glacier and monitored a 9 m<sup>2</sup> surface  
 171 observation plot with a time lapse camera array. The summer melt  
 172 season at the site is characterised by persistent positive air temperatures  
 173 typically lasting for ~60 days, from mid-June to mid-August (Rutter *et al.*,  
 174 2011). However, as is typical in western Svalbard, cloud cover occurs for  
 175 at least 55% of the summer season, and snowfall is not uncommon  
 176 (Hanssen-Bauer *et al.* 1990). In 2011, residual seasonal snow remained  
 177 across much of the Lower Foxfonna glacier surface until mid-July, with the  
 178 subsequent decay of slush over 3 days exposing superimposed ice and  
 179 glacier ice over the lower elevations from around July 21 (Day of Year  
 180 (DOY) 202).



181  
 182 **Figure 1:** (A) Map detailing Lower Foxfonna's setting and topography,  
 183 and the locations of the 9 m<sup>2</sup> observation plot with a time lapse camera  
 184 array, the automatic weather station (AWS), and the TinyTag air  
 185 temperature stations during 2011. The background orthophoto from 2006  
 186 was made available by Store Norske Spitsbergen Kulkompani AS.  
 187 Foxfonna's location in central west Svalbard is shown in the inset. (B)  
 188 Image of the observation plot, looking up-glacier, illustrating the  
 189 convergent camera set-up and reference markers with approximate scales

190 and distances shown for the arbitrary coordinate system employed (photo  
191 credit: Arwyn Edwards).

## 192 **2.2 Hydrometeorological data collection**

193 Local meteorology for the study site was recorded at an automatic  
194 weather station (AWS) installed at 601 m a.s.l. on Lower Foxfonna. The  
195 Campbell Scientific AWS recorded incident radiation ( $SW_{in}$ :  $\pm 10\%$ ), the 2  
196 m air air temperature ( $T_a$ :  $\pm 0.35^\circ\text{C}$ ), wind speed ( $\pm 0.3 \text{ ms}^{-1}$ ) that was  
197 assumed to be dominantly katabatic and down-glacier, relative humidity  
198 ( $\pm 6\%$ ), and the distance-to-ice-surface ( $\pm 0.4\%$ ) using a  $22^\circ$  field-of-view  
199 ultrasonic depth sounder. All meteorological data were logged as hourly  
200 averages of 1 min measurement sampling, and distance-to-ice was  
201 recorded discretely each hour as the mean of 10 pulses. All sensors were  
202 maintained at heights of between 1.5 and 2.5 m above the ice surface. To  
203 eliminate noise in the ultrasonic sensor record, a simple 6-hour running  
204 mean was used to smooth the ice ablation data, following application of  
205 the manufacturer's temperature correction factor. Precipitation (with an  
206 accuracy of  $\pm 8\%$ ) was acquired at 12-hour intervals from  $\sim 18$  km north-  
207 west of Foxfonna at Svalbard Lufthaven (available at [www.eklima.no](http://www.eklima.no)).

208 From the AWS data, we estimated the energy balance at our observation  
209 plot following Brock and Arnold's (2000) point-based approach adjusted  
210 for high latitudes (see Irvine-Fynn *et al.*, 2014b). Briefly, the model  
211 estimates net short- and long-wave radiation, sensible heat, and latent  
212 heat fluxes at a point at hourly time-steps using inputs of observed  
213 irradiance, air temperature, windspeed and derived saturated vapour  
214 pressure. Additional geometric data (e.g., latitude, elevation, slope, and  
215 aspect), elevation difference between point of interest and the location of  
216 the input meteorological records, and ice albedo and aerodynamic  
217 roughness can be prescribed. Subsurface heat conduction is excluded  
218 from the model. Incident radiation and wind speed at the AWS were  
219 assumed to be representative for our observation plot, particularly as  
220 terrain shadowing is not explicitly accounted for, while saturation vapour  
221 pressure was assumed to hold an empirical relationship with relative  
222 humidity and air temperature (Irvine-Fynn *et al.*, 2014b). To describe the  
223 air temperature at the plot elevation of  $\sim 492$  m a.s.l., we employed three  
224 Gemini TinyTag air temperature loggers in aspirated housings (precision:  
225  $\pm 0.4^\circ\text{C}$ ) over the lower part of the glacier (see Figure 1). From DOY 200  
226 to 240, hourly  $T_a$  and the three TinyTag records were highly correlated  
227 ( $0.844 < r < 0.961$ ;  $p < 0.05$ ), and revealed a mean linear lapse rate of  $-$   
228  $0.011 \text{ }^\circ\text{C m}^{-1}$  at the hourly time-step between 454 and 601 m a.s.l.. Air



229 temperature at the observation plot was estimated from  $T_a$  using a time-  
230 varied, linear lapse rate derived for each hour.

231 Advancing the energy balance model to incorporate time-evolving surface  
232 properties, we incorporated our photogrammetric data to describe the  
233 albedo ( $\alpha$ ) and aerodynamic roughness ( $z_0$ ) at the observation plot (see  
234 Section 2.4). Lastly, while anticipated to be small, we estimated the  
235 additional melt generated by precipitation at the plot using the regional  
236 17.5% per 100 m lapse rate (van Pelt *et al.*, 2016). We assumed that  
237 over the twelve-hour measurement intervals, precipitation fell at (i) a  
238 steady rate, and (ii) the corresponding positive mean 2 m air temperature  
239 at the observation plot; we discounted precipitation during periods where  
240 air temperatures were  $\leq 0$  °C (see Hock, 2005).

### 241 **2.3 Digital image acquisition and photogrammetric processing**

242 At the subjectively typical mid-glacier plot site, we targeted the  
243 transitional time-period that follows the demise of seasonal snow-cover,  
244 as residual snow and superimposed ice degrades, and bare glacier ice is  
245 exposed and subject to increased melt. We advanced the image  
246 acquisition methods described by Irvine-Fynn *et al.* (2014a) to record the  
247 evolving ice surface topography. Specifically, three 14 Mpix Pentax Optio  
248 WG-1 cameras in time-lapse mode were installed to provide red-green-  
249 blue (RGB) stereo images of the observation plot, with redundancy  
250 (Figure 1B). The Optio cameras capture  $4288 \times 3216$  pixel JPEG images  
251 with a bit depth of 24, using a CCD sensor ( $6.2 \times 4.6$  mm) with a focal  
252 length range of 28 to 140 mm and maximum aperture of F3.5–5.5. The  
253 cameras were mounted on wooden poles  $\sim 0.95$  m apart, drilled into the  
254 ice to depth of  $\sim 1.5$  m, and oriented up-glacier with convergent optical  
255 axes  $\sim 45^\circ$  from nadir to minimize camera calibration errors (Wackrow  
256 and Chandler, 2008). Images were captured automatically every hour  
257 over a 4-week period from July 27 to August 22 (DOY 208–234), using  
258 auto-focus mode with an auto-digital ISO 80-400 setting, amplified  
259 sharpness, and no flash.

260 An important requirement of photogrammetry is the placement of ground  
261 control points (GCPs) within the overlapping camera field of view. The  
262 GCPs account for any movement in the cameras as well as tying the  
263 resulting digital surface models (DSMs) to a defined coordinate system.  
264 As there was no stable surface on which to install GCPs, an arbitrary  
265 coordinate system was defined using a taut level string affixed  $\sim 0.5$  m  
266 above the ice surface between the northern-most camera pole and two  
267 plastic poles drilled into the ice at 3 m spacing and surrounding the  
268 observation plot. Markers were then placed every 0.5 m along the string

269 and used as control points (Figure 1b). This rudimentary approach  
270 provided a simple way to tie our models to this arbitrary coordinate  
271 system; however, any movement of the poles over time would cause  
272 deviations in the GCP positions that would translate into absolute  
273 positional errors in the derived DSMs. While we mitigated these errors by  
274 monitoring and re-surveying the GCP positions regularly (every two to  
275 three days), their influence on our results was expected to be minimal  
276 since our analysis focused only on relative changes in surface relief.  
277 Moreover, any GCP drift caused by ice ablation would be gradual over  
278 time and thus errors between sequential models would be small even if  
279 the GCP movement was significant over time. Finally, while placement of  
280 all GCPs on the same plane is not ideal, robust camera calibration and  
281 tightly constraining the models to the encompassing GCP network helped  
282 to maximize the relative quality of neighbouring DSMs in the time series,  
283 though this is more important for change detection analysis than for  
284 comparisons of surface roughness. We anticipated and found that these  
285 surface changes and the relief were large compared to any resulting  
286 relative error in the DSMs (see below).

287 Ice ablation during the observation period necessitated adjustment of the  
288 time lapse camera array on Aug 1 and 13 (DOY 213 and 225): these  
289 major amendments in GCP geometry were recorded manually with an  
290 estimated uncertainty of 5 mm and 2°. Owing to a combination of misty  
291 conditions or snow and camera lens icing that reduced visibility in the  
292 images, and camera tilt that became problematic for adequately resolving  
293 the GCPs, imagery between Aug 5 and 12 (DOY 217 and 224) was  
294 discarded from the analyses. Following initial photogrammetric checks,  
295 optimal lighting conditions for derivation of DSMs and orthomosaics were  
296 found to be at 18:00 local time, and so one DSM was generated per day  
297 at this time.

298 Camera calibration and photogrammetric processing to produce the DSMs  
299 from the time-lapse imagery were undertaken in Topcon's ImageMaster  
300 Pro. For further details on oblique photogrammetric processing, see Wolf  
301 and Dewitt (2000). Without independent means of measuring the ice  
302 surface topography or GCP geometry, it was not possible to fully quantify  
303 error in the DSMs. However, the block (or bundle) adjustment results  
304 provide an indication of the photogrammetric fit to the final rasterized  
305 solution. Here, mean horizontal DSM fit was estimated to be ~2 mm with  
306 resolution along the optical axis of 2 mm. Vertical precision was lower,  
307 and also included the millimetre-scale catenary error associated with the  
308 control point set-up (Irvine-Fynn *et al.*, 2014a). Nonetheless, with the  
309 source image resolution, we estimated that a conservative, vertical sub-

310 centimetre uncertainty remained (see Irvine-Fynn *et al.*, 2014a; Smith  
311 and Vericat, 2015), which lay below the anticipated daily ablation (Rutter  
312 *et al.*, 2011). The DSMs were resampled to a 5 mm horizontal resolution  
313 across the observation plot.

#### 314 **2.4 Derivation of glacier surface metrics**

315 To describe the changing morphology of a  $1.5 \times 1.5$  m ( $2.25$  m<sup>2</sup>)  
316 common area across the 17 rasterized DSMs that were generated for the  
317 observation plot, using a kernel equivalent to  $5 \times 5$  pixels ( $0.025$  m  
318 resolution or  $1 \times 10^{-4}$  m<sup>2</sup>) we extracted three roughness metrics,  
319 averaged across the plot: the relative position of topography (Jenness,  
320 2006), standard deviation of elevations (Ascione *et al.*, 2008), and Riley's  
321 terrain ruggedness index which describes the elevation difference  
322 between adjacent DSM cells (Riley *et al.*, 1999).

323 For comparison, we then extracted elevation data profiles from the  
324 common area, oriented cross- and down-glacier at 5 mm intervals. Each  
325 individual profile was linearly detrended, and the following standard soil  
326 science roughness metrics were calculated, then averaged for the plot  
327 (after Irvine-Fynn *et al.*, 2014a): the standard error of elevation or  
328 effective roughness height (the random roughness: Allmaras, 1966); the  
329 absolute sum of slopes (Currence and Lovely, 1970); and a microrelief  
330 index that is based on the maximum angle from the horizontal between  
331 measured elevation points (Romkens and Wang, 1987). In glaciology, the  
332 bulk aerodynamic approach that uses topographic profiles and Lettau's  
333 (1969) physical approximation (see Munro, 1989; Brock *et al.*, 2006) is a  
334 commonplace and satisfactory approach (Chambers *et al.*, 2019) to  
335 estimate  $z_0$ . Therefore, we also derived roughness lengths ( $z_{0M}$ ) from the  
336 detrended across- and down-glacier profiles. Negligible difference in the  
337 magnitude and patterns retrieved for each of the topographic metrics was  
338 found following a reduction of the data sampling resolution to 10 mm,  
339 corresponding to the finest resolution required for adequate  
340 representation of roughness (Rees and Arnold, 2006).

341 Removal of larger-scale trends (e.g., overarching plot slope) is crucial for  
342 more robust evaluations of surface roughness (James *et al.*, 2007).  
343 Therefore, to further our analyses, we used a two-dimensional linear  
344 detrend to remove overarching surface slope signatures for each DSM.  
345 From each of these detrended DSMs, we calculated the Bearing Area  
346 Curve, which is the cumulative distribution function of the detrended  
347 elevations, and derived a z-score histogram. Lastly, following the 2-  
348 dimensional method detailed in Smith *et al.* (2016), we determined two  
349 cross- and two down-glacier estimates for each DSM, which accounts for

350 upwind frontal area to calculate an alternative aerodynamic roughness  
351 estimate ( $z_{0S}$ ). Assuming  $z_{0S}$  to be a more robust measure of the bulk  
352 aerodynamic roughness compared to  $z_{0M}$  (see Smith *et al.*, 2016), we  
353 then used these mean cross- and down-glacier metrics for each DSM to  
354 derive a surface anisotropy index ( $\Omega$ : after Smith *et al.* (2006)).

355 To examine the frequency and orientation of any glacier surface  
356 roughness signals in the detrended DSMs, we applied long-standing  
357 spectral and geostatistical approaches (e.g., Mulla, 1988; Hertzfeld *et al.*  
358 2000; Rees and Arnold, 2006). Firstly, we employed a two-dimensional  
359 fast Fourier transform to retrieve a frequency domain depiction of the  
360 amplitude of topographic variations in cross- and down-glacier directions  
361 (e.g., Perron *et al.*, 2008; Spagnolo *et al.*, 2017); the detrended DSM  
362 data were used without further adjustment or filtering. Subsequently, we  
363 computed the overall spatial autocorrelation (or omnidirectional  
364 semivariograms) from detrended elevation values extracted from 2000  
365 randomly located points distributed across each of the detrended DSMs.  
366 For comparison, each of the semivariograms were normalized to the  
367 associated detrended elevation variance. The analysis was restricted to a  
368 maximum lag distance of  $\sim 0.75$  m, as defined by the plot scale. Guided  
369 by the results of the Fourier transform (see Section 3.2), to explore  
370 directional contrast in spatial autocorrelation, we recalculated directional  
371 semivariograms for each of the DSMs using the two, perpendicular  
372 directions of cross- and down-glacier, with a  $30^\circ$  tolerance.

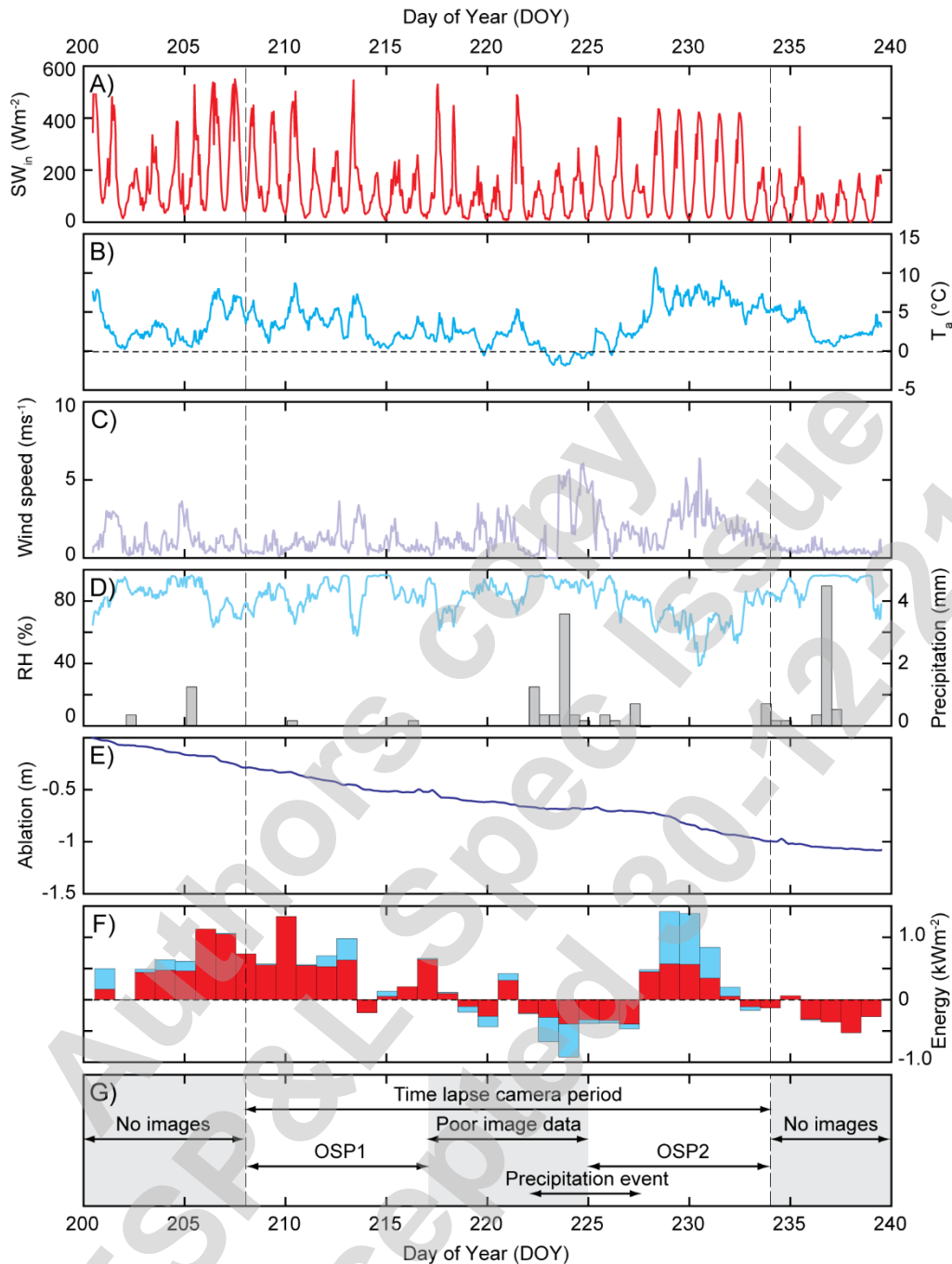
373 To enhance the energy balance modelling at the observation plot using a  
374 temporally varying albedo, we determined the apparent cryoconite area  
375 with *ImageJ* software (Schneider *et al.*, 2012), using pixel thresholding of  
376 the blue band of the daily orthophotographs (see Irvine-Fynn *et al.*,  
377 2011). The apparent cryoconite area was converted to an albedo proxy  
378 following the relationship reported by Irvine-Fynn *et al.* (2011) for  
379 Longyearbreen, a similarly north-facing glacier proximate to Foxfonna;  
380 cubic interpolation of these discrete, daily time-points provided an hourly  
381 estimate of surface albedo at intervals, and the observed mean of 0.62  
382 was used for the periods before and after the time-lapse imaging. With  
383 knowledge that katabatic winds are dominant across Lower Foxfonna  
384 (unpublished data), we prescribed a time-varied aerodynamic roughness  
385 length in the model using the mean plot-scale cross-glacier profile ( $z_{0M}$ ) at  
386 18:00 each day, estimating  $z_0$  at hourly time-steps over the observation  
387 period with a cubic interpolation. For the time-periods before and after  
388 the imaging periods,  $z_0$  was fixed as the mean DSM-derived cross-glacier  
389  $z_{0M}$ . We note that our time-varying estimates of albedo and roughness are  
390 not fully validated, and so while representing 'best estimates' they  
391 introduce some uncertainty in the melt model outputs.

### 392 **3. RESULTS**

#### 393 **3.1 Lower Foxfonna's hydrometeorology**

394 Figure 2 summarises the summertime meteorological conditions on Lower  
395 Foxfonna in 2011. Over the imaging period,  $T_a$  remained low with a mean  
396 of  $3.4^\circ\text{C}$ , and 52% of the days being classed as cloudy with maximum  
397 daily  $\text{SW}_{\text{in}} < 400 \text{ Wm}^{-2}$ . Ice ablation at the AWS typically reached  $27 \text{ mm}$   
398  $\text{d}^{-1}$  ( $0.025 \text{ m w.e. d}^{-1}$ ). The observation period was characterised by two  
399 phases separated by a precipitation event (DOY223–224): the first phase  
400 becoming increasingly overcast over time, with declining air temperature,  
401 low wind speed, and high humidity (DOY 208–222); the second, with  
402 rising irradiance and air temperature, elevated winds, and comparatively  
403 lower humidity (DOY225–234). These two contrasting phases also broadly  
404 coincided with the two sets of reconstructed DSMs derived from the plot,  
405 hereafter referred to as Observation Subperiods (OSP) 1 and 2. Both  
406 imaging periods began with discrete patches of residual snow on the  
407 glacier surface that took approximately 48 hrs to clear and expose bare-  
408 ice.

409 The numerically simulated melt over 12-hr periods, corresponding to the  
410 precipitation record interval, was highly correlated to observed ablation ( $r$   
411  $= 0.97$ ). Advected energy from rainfall was negligible, accounting for less  
412 than  $0.1 \text{ mm w.e. d}^{-1}$ , owing to low air temperature and temporally  
413 averaged precipitation intensity. OSP1 was characterised by proportionally  
414 high radiative fluxes (Figure 2G), with only minor contributions from  
415 turbulent energy, because although air temperatures were relatively high  
416 ( $T_a \approx 5^\circ\text{C}$ ), wind speeds remained low (typically  $< 2 \text{ m s}^{-1}$ ). In the latter  
417 stages of OSP1, melt rates declined from DOY 214–216 as both incident  
418 radiation and air temperature declined. In contrast, OSP2 began with 3  
419 days of net energy loss by the glacier (i.e. no melt), and the following five  
420 days (DOY228–232) exhibited more balanced contributions to ablation  
421 from radiative and turbulent energy fluxes, with elevated air temperature  
422 ( $T_a < 5^\circ\text{C}$ ) and wind speed ( $\sim 2.5 \text{ m s}^{-1}$ ), which subsequently declined.



423

424

425

426

427

428

429

430

431

432

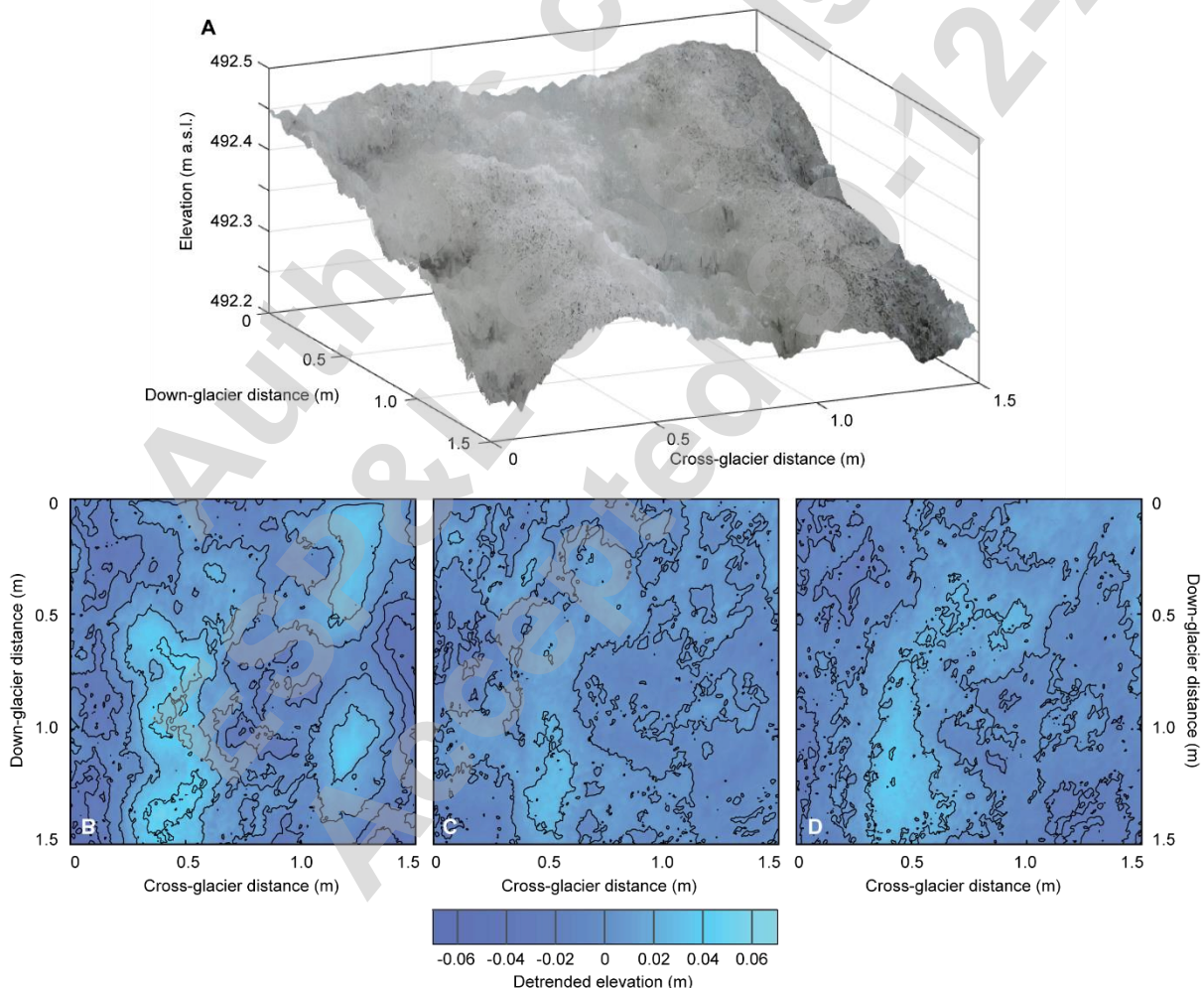
**Figure 2:** Time-series of hydrometeorological conditions at the observation plot on Lower Foxfonna, illustrating: (A) incident radiation,  $SW_{in}$ ; (B) air temperature at 2 m,  $T_a$ ; (C) wind speed; (D) relative humidity (RH) and precipitation; (E) cumulative ice ablation; (F) modelled surface energy balance, with bars indicating total daily energy receipt separated into radiative (red) and turbulent (blue) fluxes, with negative values indicative of periods exhibiting energy lost from the glacier to the atmosphere; and (G) schematic chart of image data acquisition, the two OSPs and notable meteorological phases.

433

### 3.2 Fine-scale surface topography and roughness

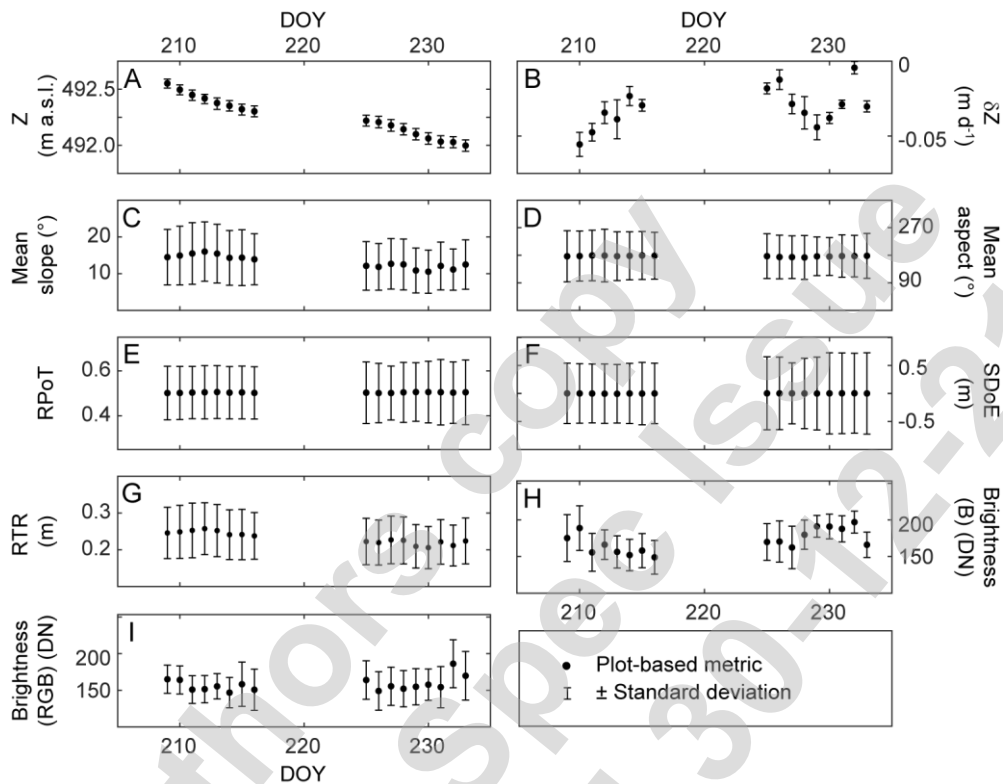
434 Our photogrammetric approach yielded 17 fine-scale DSMs and  
 435 orthomosaics describing the ice surface at the observation plot (Figure  
 436 3A). Throughout the DSM time-series, the ice surface topography  
 437 changed (Figures 3B-D). The seventeen 5 mm horizontal resolution DSMs  
 438 revealed the plot was typically characterised by a mean relief of 0.26 m,  
 439 with a standard deviation of 0.055 m. Daily differencing of the DSMs over  
 440 the common area showed a maximum elevation change of  $-0.115 \text{ m d}^{-1}$ ;  
 441 however, recognising the spatial uncertainties within the DSMs, using a  
 442  $5 \times 5$  pixel kernel, the mean relief decreased to  $0.24 (\pm 0.055) \text{ m}$  with a  
 443 maximum ablation of  $0.092 \text{ m w.e. d}^{-1}$ . Across the common area over the  
 444 observation period, the DSMs revealed a mean ablation of  $0.028 \text{ m w.e. d}^{-1}$   
 445 (Figures 4A, 4B), which equalled that reported at the weather station  
 446 (Section 3.1; Figure 2E).

447



448 **Figure 3:** (A) Example three-dimensional visualisation of the  $2.25 \text{ m}^2$   
 449 observation plot for DOY213 retrieved following our photogrammetric  
 450 workflow; the 5 mm resolution DSM, with vertical exaggeration, is  
 451 overlain by the coincident 2 mm orthomosaic and highlights fine-scale  
 452

453 morphology and the presence of impurities across the plot. Shaded  
 454 contour plots for the two-dimensionally detrended DSMs retrieved for (B)  
 455 DOY213, (C) DOY225, and (D) DOY233 illustrating the evolving  
 456 topography of the bare-ice surface. Note the reduction in plot's  
 457 topography between 1.0 and 1.5 m in the cross-glacier direction.



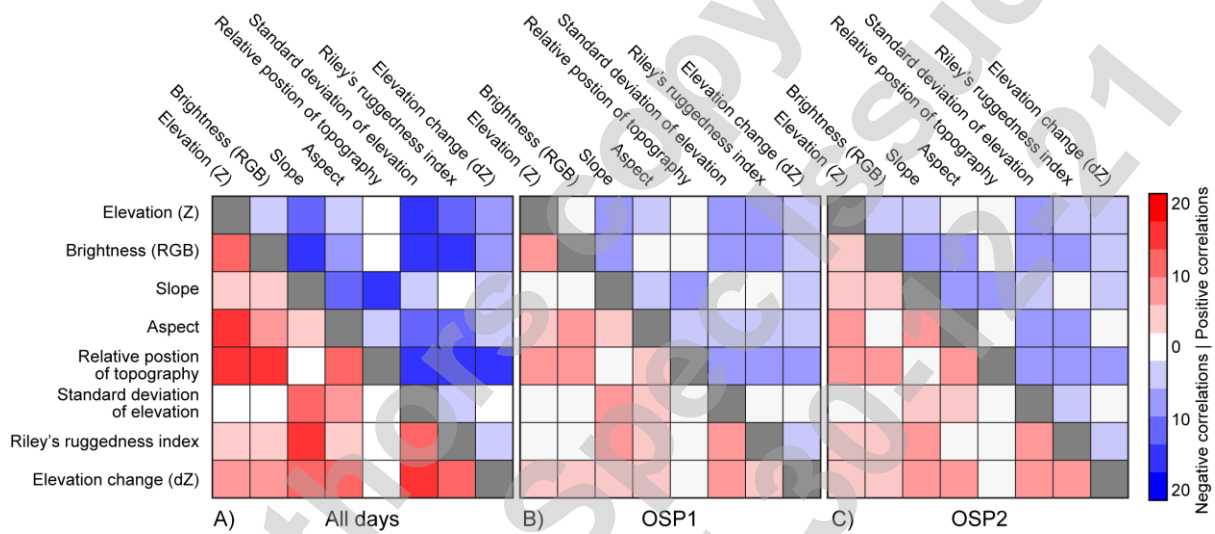
458

459 **Figure 4:** Kernel-based elevation, roughness and brightness metrics  
 460 across the observation plot, and their variation over time during OSP1  
 461 and OSP2. (A) Surface elevation based on GCPs for OSP1 and OSP2,  
 462 noting the elevation data is not continuous between the OSPs; (B)  
 463 ice surface elevation change for the preceding 24-hour period; (C) mean  
 464 surface slope over the observation plot; (D) mean surface aspect; (E)  
 465 position of topographic roughness, RPoT; (F) standard deviation of  
 466 elevation, SDoE; (G) Riley's topographic ruggedness index, RTR; (H)  
 467 blue-band orthomosaic brightness reported as a digital number (DN); and  
 468 (I) RGB orthomosaic brightness (DN). Error bars are given as  $\pm 1 \times$   
 469 standard deviation.

470 The mean DSM pixel scale slope varied over a  $5.5^\circ$  range throughout the  
 471 OSPs, but the mean aspect and the traditional kernel-based  
 472 morphological metrics remained constant over time (Figures 4C-F). Owing  
 473 to its dependence on kernel-scale slope, Riley's topographic ruggedness  
 474 index showed subtle variation centred at  $\sim 0.23$  m (Figure 4G). As source  
 475 images were not colour-calibrated and the camera automatically adjusted  
 476 the F-stop, ISO and exposure time, the temporal pattern in the RGB  
 477 brightness was challenging to interpret (Figure 4I); however, the blue-



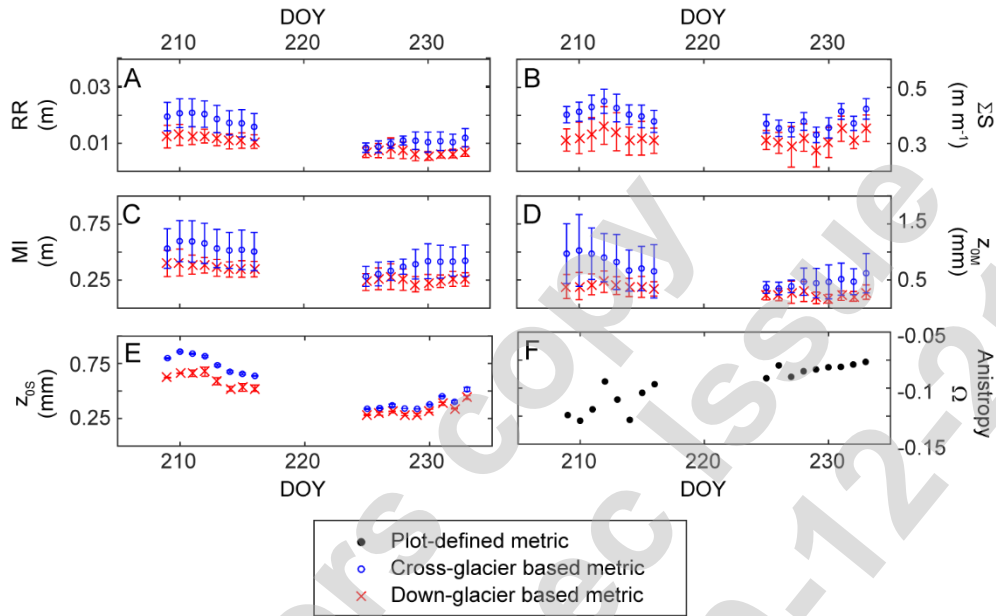
478 band brightness, as an albedo proxy (see Irvine-Fynn *et al.*, 2011),  
 479 suggested a declining surface reflectance during OSP1, and subsequently  
 480 a subtle increase during OSP2 (Figures 4H). For the individual DSMs,  
 481 correlations between kernel-based surface descriptors and the associated  
 482 melt rate were generally weak ( $|r| < 0.1$ ) but highly varied, with both  
 483 positive and negative spatial correlations ( $-1 < r < 0.98$ ) depending on  
 484 the day of observation, and with no identifiable difference between OSP1  
 485 and OSP2 (Figure 5). Elevation change at the kernel-scale, between  
 486 sequential DSMs, was not consistently correlated to any ice surface  
 487 descriptor for the first DSM of each pair (Figure 5).



488  
 489 **Figure 5:** Illustration of the number of positive and negative correlations  
 490 between all of the kernel-based DSM surface metrics and surface change  
 491 (dZ) for (A) the observation period, (B) OSP1 and (C) OSP2.

492 The variability in surface topography and roughness (Figure 3) over the  
 493 OSPs was better evidenced by the profile-based metrics, with directional  
 494 difference evident between the cross- and down-glacier directions  
 495 (Figures 6A-6E). The cross-glacier random roughness and microrelief  
 496 indices were 17% to 88% greater than their counterparts oriented down-  
 497 glacier; for  $z_{0M}$  this directional contrast was greater at 38% to 180%.  
 498 These relative directional disparities were most pronounced during OSP2  
 499 (from DOY229). A similar contrast was seen in  $z_{0S}$ , with down-glacier  
 500 values being 17% to 30% greater than the across-glacier direction. With  
 501 the exception of the sum of slopes, temporal decline characterised the  
 502 cross-glacier profile-based roughness metrics over the OSP1, which then  
 503 increasing during OSP2. The  $\Sigma S$  metric lacked clear, systematic variations  
 504 over time which suggested that the surface texture remained broadly  
 505 similar throughout the OSPs. The detrended DSMs revealed the

506 observation plot surface was weakly anisotropic, with cross-glacier  
 507 roughness  $z_{0S}$  consistently greater than equivalent down-glacier values ( $-$   
 508  $0.13 < \Omega < -0.07$ ). A seasonal trend in  $\Omega$  with a significant increase over  
 509 time ( $r^2 = 0.79$ ;  $p < 0.01$ ;  $n = 17$ ) showed the surface became  
 510 progressively more isotropic (Figure 6F).



511

512 **Figure 6:** Profile-derived and two-dimensional roughness metrics, and  
 513 their variation over time. (A) random roughness, RR; (B) absolute sum of  
 514 slopes,  $\Sigma S$ ; (C) microrelief index, MI; (D) profile-based bulk aerodynamic  
 515 roughness estimate,  $z_{0M}$ ; (E) two-dimensional aerodynamic roughness  
 516 estimate,  $z_{0S}$ ; and (F) anisotropic index derived from cross- and down-  
 517 glacier  $z_{0S}$ . Error bars are given as  $\pm 1 \times$  standard deviation.

518 Examining the time-series of roughness metrics (Figures 4 and 6), of the  
 519 kernel-based metrics, only the Riley's ruggedness index showed strong,  
 520 positive association with the profile-based cross-glacier roughness metrics  
 521 ( $0.74 < \rho < 0.84$ ;  $p < 0.01$ ). The cross-glacier profile-based metrics were  
 522 all positively correlated: Spearman's  $\rho > 0.77$ ,  $p < 0.01$ . Speculating that  
 523 glacier roughness increases under radiative-driven melt, and decreases  
 524 under turbulent fluxes (Muller and Keeler, 1969), from the melt model  
 525 output we derived these two cumulative energy fluxes for 24-hour  
 526 intervals preceding each DSM, and the associated turbulent:radiative  
 527 energy flux ratio. Riley's ruggedness metric, and profile-derived random  
 528 roughness, microrelief index, and both  $z_0$  metrics were all significantly  
 529 correlated to both the daily cumulative radiative energy ( $0.31 < \rho < 0.66$ ;  
 530  $p < 0.05$ ), and the blue-band brightness ( $0.60 < \rho < 0.93$ ;  $p < 0.02$ ).  
 531 However, only the kernel-based relative position of topography metric

532 showed significant association with cumulative turbulent energy and the  
 533 turbulent:radiative energy ratio.

534 **Table 1:** Correlation matrix for daily energy flux proxies and mean  
 535 observation plot roughness measures. Correlations are reported with the  
 536 Spearman's  $\rho$ -value, and those which are significant at the 95%  
 537 confidence level are italicised and shaded. Cumulative incident radiation  
 538 and turbulent energy, and the turbulent:radiative energy flux ratio for the  
 539 24-hour periods between each DSM are denoted  $\Sigma\text{Rad}_{24}$ ,  $\Sigma\text{Turb}_{24}$  and  
 540  $[\text{T}:\text{R}]_{24}$ , respectively. Brightness was extracted from both the RGB and  
 541 blue-band orthomosaics of the observation plot.

542

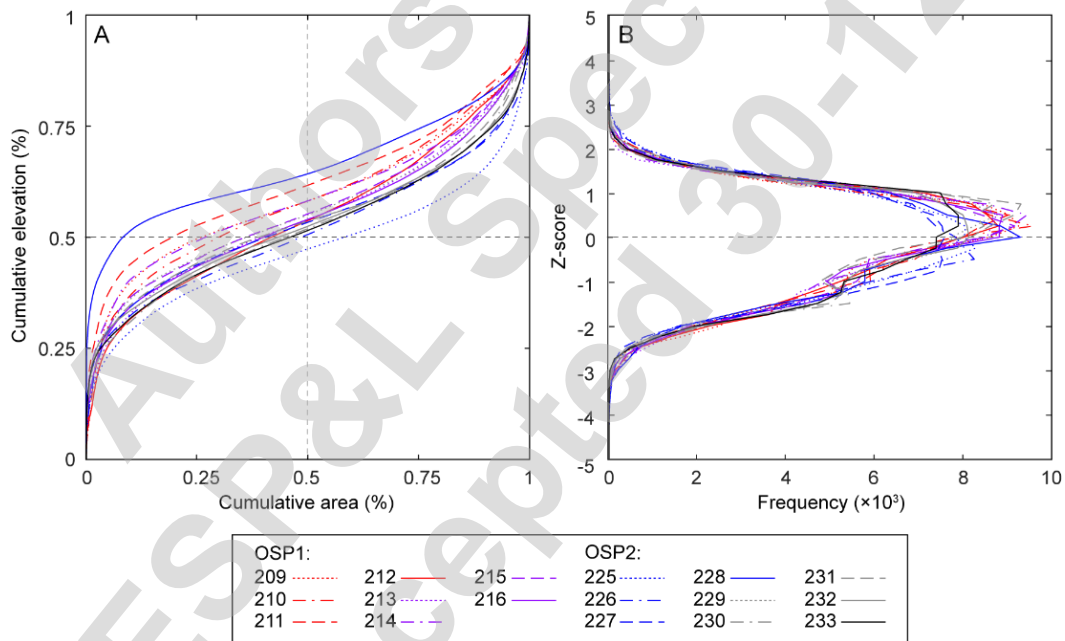
|                                 | $\Sigma\text{Rad}_{24}$ | $\Sigma\text{Turb}_{24}$ | $[\text{T}:\text{R}]_{24}$ | Brightness (RGB) | Brightness (blue) |
|---------------------------------|-------------------------|--------------------------|----------------------------|------------------|-------------------|
| $\Sigma\text{Turb}_{24}$        | 0.19                    |                          |                            |                  |                   |
| $[\text{T}:\text{R}]_{24}$      | <i>0.60</i>             | <i>0.59</i>              |                            |                  |                   |
| Brightness (RGB)                | 0.09                    | -0.04                    | 0.06                       |                  |                   |
| Brightness (blue)               | <i>0.65</i>             | 0.01                     | 0.17                       | 0.03             |                   |
| Relative position of topography | 0.42                    | <i>0.72</i>              | <i>0.71</i>                | 0.02             | 0.05              |
| Standard deviation of elevation | -0.31                   | -0.06                    | -0.10                      | 0.45             | <i>-0.49</i>      |
| Riley's topographic ruggedness  | 0.31                    | -0.36                    | -0.26                      | -0.17            | <i>0.70</i>       |
| Random roughness                | <i>0.61</i>             | -0.17                    | 0.08                       | -0.11            | <i>0.85</i>       |
| Sum of slopes                   | 0.38                    | 0.00                     | -0.02                      | -0.07            | <i>0.60</i>       |
| Microrelief index               | <i>0.66</i>             | -0.07                    | 0.10                       | 0.02             | <i>0.92</i>       |
| $z_{0M}$                        | <i>0.60</i>             | -0.18                    | 0.07                       | 0.08             | <i>0.90</i>       |
| $z_{0S}$                        | <i>0.50</i>             | -0.17                    | -0.11                      | -0.01            | <i>0.88</i>       |
| Anisotropy, $\Omega$            | -0.39                   | 0.44                     | 0.19                       | 0.18             | <i>-0.72</i>      |

543

544 Once bare-ice was exposed in OSP1,  $z_{0M}$  decreased over time ( $r^2 = 0.87$ ;  
 545  $p < 0.01$ ), but this was coincident with a decline in the radiative energy  
 546 over the same timescale ( $r^2 = 0.44$ ;  $p < 0.05$ ). Conversely, over OSP2,  
 547  $z_{0M}$  increased ( $r^2 = 0.77$ ;  $p < 0.01$ ) but concurrent increases in daily  
 548 radiative or turbulent fluxes were insignificant ( $r^2 < 0.08$ ;  $p > 0.2$ ). The  
 549 temporal trends in  $z_{0S}$  were similarly significant in both OSPs. During  
 550 OSP1, the difference between cross- and down-glacier  $z_{0M}$  decreased by

551 0.05 mm d<sup>-1</sup> indicative of a smoothing of the ice surface; for z<sub>0S</sub>, this  
 552 decline was 0.025 mm d<sup>-1</sup>. In comparison, during OSP2 the directional  
 553 difference rose by only 0.03 mm d<sup>-1</sup> for z<sub>0S</sub> and 0.01 mm d<sup>-1</sup> for z<sub>0M</sub>.

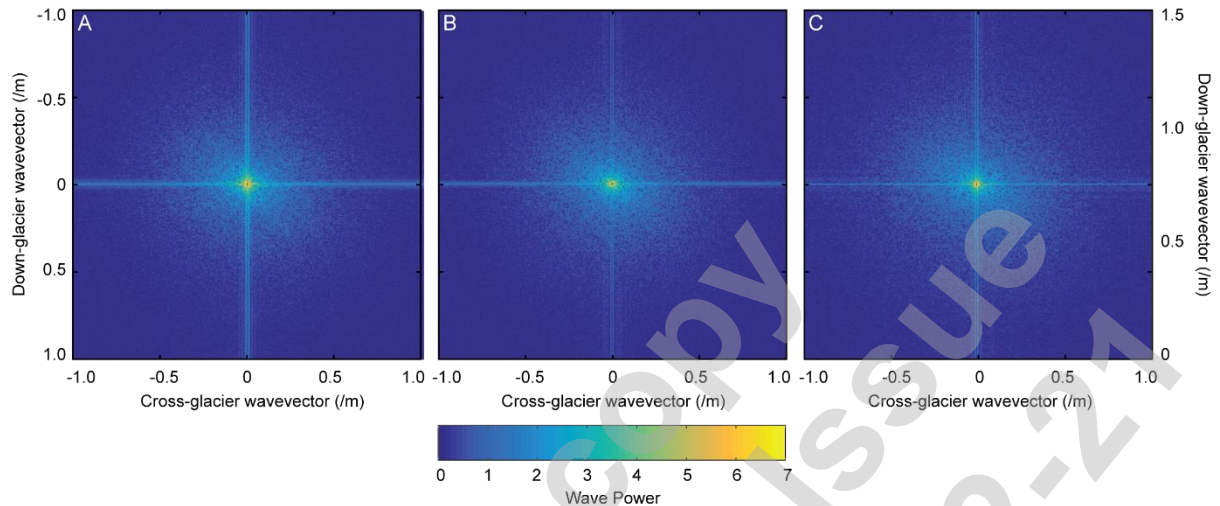
554 The Bearing Area Curves (Figure 7A) showed a broad similarity in form,  
 555 typically with the lower 50% of the detrended elevation range occupying  
 556 only between 19% and 47% of the total area, with exception to the two  
 557 outmost curves (DOY225 and 228). The slightly positive elevation skew  
 558 revealed by the Bearing Area Curves was clear in the corresponding z-  
 559 score histograms (Figure 7B): a z-test confirmed that all the detrended  
 560 DSMs statistically followed a normal distribution ( $|z| < 1.15 \times 10^{-11}$ ;  $p <$   
 561  $0.01$ ) although there is a higher probability that a point in the detrended  
 562 DSM surface lies between 0 and +1 standard deviation of the detrended  
 563 elevation range, equivalent to approximately 0 to 16 mm above the  
 564 generalised mean surface plain. There was some variability seen in the z-  
 565 score plot suggestive of topographic variability at intermediate depths  
 566 (0.8 to 32 mm) below the generalised surface plane.



567  
 568 **Figure 7:** (A) Bearing Area Curves for each detrended DSM and (B)  
 569 detrended DSM z-score histograms, showing an absence of any  
 570 systematic change over time. Curves are plotted for each of the 17  
 571 detrended DSMs, indicated for each DOY.

572 The two-dimensional Fourier transform consistently showed highest power  
 573 in the centre of the Fourier domain (Figure 8), corresponding to low  
 574 frequency signals and gradual changes in the glacier surface topography.  
 575 Critically, the orientation of any dominant periodicity in the topography  
 576 would produce perpendicular lines in the Fourier power plots. The absence  
 577 of any oblique patterns in the Fourier power surfaces (Figure 8),

578 suggested topographic periodicity in the detrended DSMs was oriented in  
579 the plot's across- and down-glacier directions. The relative power of these  
580 two perpendicular signals was reduced for DOY 225 and 233, indicative of  
581 a reduced topographic variability during OSP2.



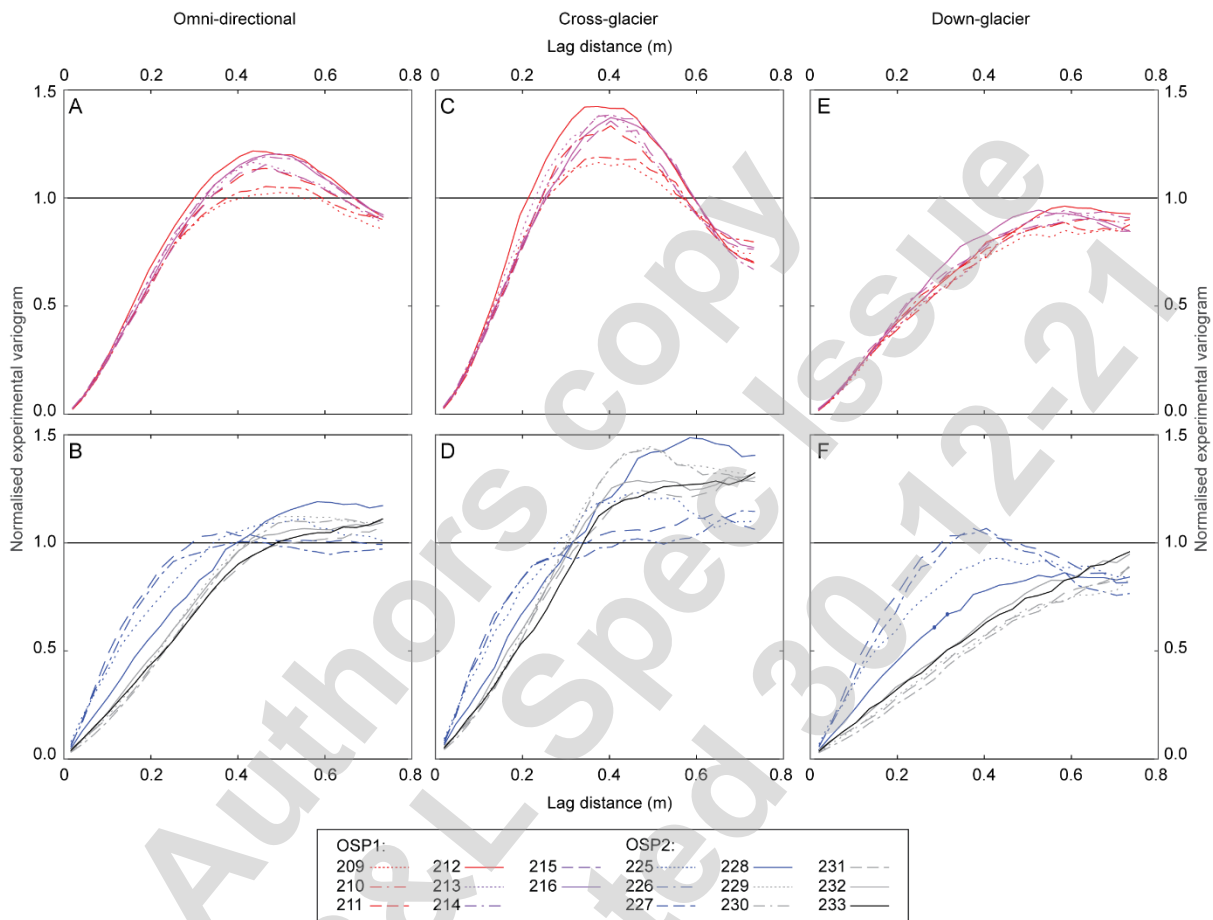
582

583 **Figure 8:** Plots of the two-dimensional Fourier transform of the  
584 detrended DSMs retrieved on (A) DOY213, (B) DOY225, and (C) DOY233,  
585 highlighting the absence of any topographic signal oblique to the cross-  
586 and down-glacier directions.

587 With regard to spatial autocorrelation in surface topography, the  
588 omnidirectional semivariograms, derived from the detrended DSMs,  
589 showed a contrast between OSP1 and OSP2 (Figures 9A and 9B). During  
590 OSP1, the semivariograms showed similar form, with a lag distance of  
591 0.43 and 0.49 m to the peak semivariance of  $0.00045 (\pm 0.0001) \text{ m}^2$ . For  
592 OSP2, the peak semivariance was reduced, at  $0.00015 (\pm 5.5 \times 10^{-5}) \text{ m}^2$ ,  
593 and the associated lag distance varied from 0.37 to  $< 0.73$  m. However,  
594 none of the individual semivariograms could be modelled using  
595 monotonically-increasing spherical, exponential or gaussian model  
596 functions (e.g., Rees and Arnold, 2006; Ryan *et al.*, 2017).

597 With roughness metrics (Figure 6) and the two-dimensional Fourier power  
598 spectrum (Figure 8) confirming the topographic signals aligned with the  
599 across- and down-glacier geometry, the directional semivariograms  
600 across- and down-plot revealed a 'hole effect' semivariogram model  
601 (Journel and Huijbregts, 1978; Pyrcz and Deutsch, 2003). During OSP1,  
602 the cross-glacier empirical semivariograms peaked at a lag distance of  
603  $\sim 0.4$  m, falling thereafter with the suggestion of a cyclical form at lag  
604 distances  $< 0.7$  m (Figure 9C); the down-glacier semivariance, in  
605 contrast, tended to approach a sill at a lag distance of  $\sim 0.5$  m (Figure  
606 9E). During OSP2, the shape of the semivariograms was less coherent,

607 with cross-glacier semivariograms continuing to increase or showing  
 608 indications of some variability at lag distances > 0.4 m (Figure 9D); in the  
 609 down-glacier direction, some days exhibited monotonic increase towards  
 610 the overall plot semivariance at ranges > 0.6 m, while others (snow-  
 611 affected DOY225-227) displayed semivariance peaks at lag distances of  
 612 ~0.4 m (Figure 9F).



613

614 **Figure 9:** Variance-normalised empirical semivariograms derived for the  
 615 detrended DSMs generated for OSP1 and OSP2: omnidirectional  
 616 semivariograms for OPS1 (A) and OSP2 (B); cross-glacier semivariograms  
 617 for OSP1 (C) and OSP2 (D); and down-glacier semivariograms for OSP1  
 618 (E) and OSP2 (F). Semivariograms are reported for each DOY within the  
 619 OSPs. Note, DOYs 209, 210, 225-227 were affected by declining patches  
 620 of residual snow over the observation plot.

#### 621 4. DISCUSSION

622 Conventional understanding of bare-ice topographic development  
 623 suggests that roughness increases over the melt season following the  
 624 elimination of seasonal snow as the ice surface degrades and supraglacial  
 625 channels and hummocks are established (Smith *et al.*, 2020). We,  
 626 therefore, examine our microtopographic data from Lower Foxfonna for  
 627 the two, contrasting time-periods, OSP1 and OSP2, within this context.



#### 628 **4.1 Hydrometeorology, ablation and roughness**

629 We observed daily bare-ice microtopography over two week-long periods:  
630 OSP1 was dominated by radiative energy fluxes, while OSP2 exhibited a  
631 higher proportion of turbulent energy fluxes, compared to OSP1. Over the  
632 full observation period, the AWS recorded ice ablation rates of 25 mm  
633 w.e. d<sup>-1</sup>. These rates were reproduced by the differencing of the time-  
634 series of photogrammetrically-derived DSMs (28 mm w.e. d<sup>-1</sup>), and  
635 demonstrated the robustness of the methodological approach,  
636 acknowledging the associated uncertainties. The ablation forecast over  
637 the same time by the point-based energy balance, despite being highly  
638 correlated to observed surface lowering, over-predicted the observed melt  
639 by ~30%. This discrepancy is explained by the cold thermal regime that  
640 Foxfonna exhibits: energy is lost to subsurface conduction (e.g., Arnold *et al.*,  
641 2006; Østby *et al.*, 2017). Such losses are not accounted for in the  
642 melt model employed to estimate radiative and turbulent energy  
643 contributions, and so are not examined further here.

644 Our analytical approach demonstrated that traditional kernel-based  
645 measures, which classed the bare-ice surface as smooth or flat, offer  
646 limited insight into spatial and temporal topographic variability that the  
647 profile-based or 2-dimensional assessments reveal. Examination of  
648 metrics derived from 1×1 to 9×9 pixel kernels emphasised that increased  
649 kernel size reduced the range and variability reported by each metric: a  
650 scale-dependent behaviour well known in geomorphology (e.g.,  
651 Brasington *et al.*, 2012). Previous work has employed an adapted  
652 standard deviation of elevation over large kernels to report glacier surface  
653 roughness (e.g., Rippin *et al.*, 2015; Rossini *et al.*, 2018). However, the  
654 potential for such measures to reveal morphological change over time is  
655 unclear. Here, particularly for bare-ice surface areas, we suggest that  
656 more thorough scaling analyses of surface roughness are needed (e.g.,  
657 Chambers *et al.*; 2021; Fitzpatrick *et al.*, 2019; Smith *et al.*, 2020).  
658 Owing to the scale-dependence of both ice roughness itself (Rees and  
659 Arnold, 2006) and traditionally employed roughness metrics, multi-scale  
660 approaches should be explored (e.g., Lindsey *et al.*, 2015, 2019),  
661 particularly to discern and describe temporal change, or relate ground  
662 validation to coarser resolution satellite data retrievals.

663 The nature of the variability of the surface topography was not readily  
664 explained by the geometries and metrics describing the DSMs or the  
665 orthomosaics, highlighting the complexity of the evolution of bare-ice  
666 topography and contrasts in the meteorology during the two OSPs.  
667 Processes such as the lateral advection and redistribution of meltwater

668 (Mantelli *et al.*, 2015; Bash and Moorman, 2020) or impurities (Irvine-  
669 Fynn *et al.*, 2011; Chandler *et al.*, 2015; Takeuchi *et al.*, 2018) occur at  
670 length-scales greater than the 25 mm kernel and over time-scales below  
671 our daily observation period. However, there were indications of the  
672 apparent influence of discrete impurities on surface roughness. The blue-  
673 band brightness typically offers strong discrimination between impurities  
674 and ice (see Irvine-Fynn *et al.*, 2010). Across the plot, Riley's topographic  
675 ruggedness, the profile-based roughness metrics, and daily radiative  
676 energy receipt and blue-band brightness changed concurrently: such an  
677 association can be explained by the melting in (or out) of impurities  
678 (Gibbon, 1979; Bøggild *et al.*, 2010; Takeuchi *et al.*, 2018) and their  
679 visibility from the oblique imaging geometry, and the presence of  
680 meltwater. This process is supported by the variability in the elevation  
681 distributions with the changes at depths of up to 60 mm from the ice  
682 surface. Such depths accord with those of small cryoconite holes and  
683 supraglacial rills observed elsewhere in Svalbard (e.g., Telling *et al.*,  
684 2012; Rippin *et al.*, 2015). Because brightness was not normalised across  
685 the orthomosaic time-series, a more robust image calibration (e.g., Ryan  
686 *et al.*, 2017) approach would be required to strengthen these tentative  
687 spatio-temporal albedo and roughness associations.

#### 688 **4.2 Aerodynamic roughness length evolution**

689 Our data revealed mean estimates of  $z_0 < 1.5$  mm, with anisotropy  
690 evident in dissimilar down- and cross-glacier evaluations, as previously  
691 reported for glacier ice (e.g., Brock *et al.*, 2006; Guo *et al.*, 2011; Irvine-  
692 Fynn *et al.*, 2014a; Smith *et al.*, 2016; Fitzpatrick *et al.*, 2019; Liu *et al.*,  
693 2020). The profile-derived and two-dimensional roughness metrics  
694 demonstrated evolution during both OSPs, with rates of change in  $z_0$  that  
695 compare well to those reported by Smith *et al.* (2020), and our data  
696 demonstrate the trajectory of roughness as the glacier surface transitions  
697 from residual snow and superimposed ice to bare-ice. To explain the  
698 decline then subsequent rise in surface roughness on Lower Foxfonna, we  
699 employ a five-stage conceptual model of the development of surface  
700 features (after Guo *et al.*, 2011; Smith *et al.*, 2020): residual, melting  
701 snow roughness increases (stage 1), then, here, following the exposure of  
702 bare-ice on DOY209,  $z_0$  initially declines (stage 2), subsequently  
703 beginning to increase as the melt season continues and bare-ice degrades  
704 (stage 3), and then progressively develops a more hummocky form  
705 (stages 4). It is unclear if our observations reveal the bare-ice's seasonal  
706 'peak roughness' (stage 5: Smith *et al.*, 2020).



707 On glaciers across Svalbard, superimposed ice commonly forms early in  
708 the melt season, and is subsequently exposed and degraded as ablation  
709 progresses (Wadhams and Nuttall, 2002). On Lower Foxfonna, in 2011,  
710 immediately prior to the demise of the snowpack in late July (DOY202:  
711 see Section 2.1) superimposed ice had formed and been preserved with a  
712 thickness of  $\sim 0.2$  m (Koziol *et al.*, 2019). This friable superimposed ice  
713 layer comprised ice lenses and cryoconite distributed below  $\sim 55\%$  of its  
714 depth. During OSP1 (stage 2), through a combination of refreezing within  
715 the degrading superimposed ice layer and the subsequent progressive  
716 exposure of the underlying glacier ice, the topography appeared to  
717 smoothen. This (stage 2) trajectory was also promoted by the  
718 simultaneous decrease in radiative energy flux, which would reduce the  
719 likelihood of differential ablation arising from impurity or ice-structural  
720 albedo-feedbacks. The elevated estimated albedo ( $\sim 0.62$ : see Section  
721 2.4) compared to more typical values of  $\sim 0.4$  for glacier ice (Cuffey and  
722 Paterson, 2010), offered further evidence of a superimposed ice  
723 dominated stage.

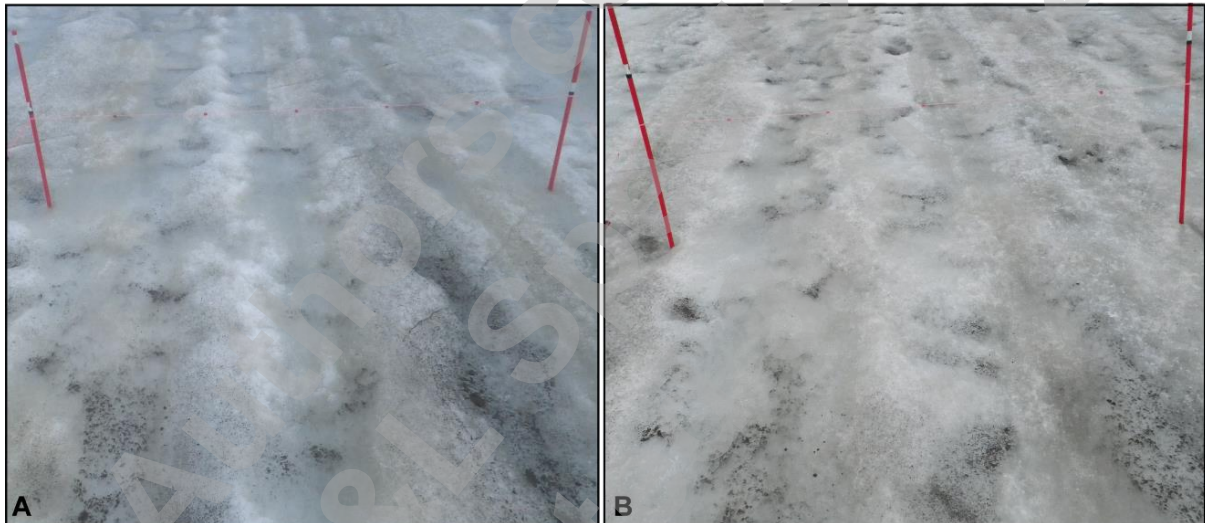
724 The timing of the precipitation event, which included snowfall at the time-  
725 lapse camera array site, and the resulting data quality issues prevented  
726 us from describing the topographic changes as superimposed ice was  
727 eliminated (stage 3). However, at the start of OSP2, residual snow cover  
728 affected the topography of the plot, most clearly evident in the Bearing  
729 Area Curve. As OSP2 progressed (stage 4), increasing roughness was  
730 driven by the sustained energy fluxes and, with turbulent fluxes  
731 dominant, spatially varied ablation arose from the surface feedbacks  
732 associated with rill development and the progressive roughening of the ice  
733 surface.

734 The importance of the observed changes in  $z_0$  were best illustrated with  
735 subsequent melt model runs, that compared the dynamic albedo and  $z_{0M}$   
736 roughness parameterisation to scenarios with  $z_0$  set as constants: using  
737 the minimum recorded across-glacier  $z_{0M}$  and  $z_{0S}$ , throughout the  
738 observation period, melt due to turbulent energy at an hourly time-scale  
739 was underestimated on average by approximately 7%, while for the  
740 equivalent maximum values this was a 10-15% overestimate. These  
741 disparities in turbulent energy fluxes translated to a typical mean  
742 uncertainty in predicted hourly ablation of up to 10%.

### 743 **4.3 Hydrological drivers of ice surface roughness**

744 Identification of the hole effect in the semivariograms derived from the  
745 detrended DSMs implies that there is an underlying form of cyclicity or  
746 structure in the topography at the plot-scale (Pyrzcz and Deutsch, 2003).

747 Here, the interpretation of the cyclical signature in the cross-glacier  
748 semivariogram, and suppressed down-glacier semivariogram, is that  
749 throughout OSP1, the glacier surface was characterised by down-glacier  
750 oriented ridges, spaced at  $\sim 0.8$  m intervals. The period was defined by a  
751 low turbulent to radiative energy ratio, and the location exhibits ice  
752 structure parallel to the surface slope, with foliation and/or antecedent  
753 topography at the observation plot broadly oriented down-glacier (Figure  
754 10A). The orientation of apparent ridges aligned with the surface slope  
755 and structure may also control: (i) the distribution of impurities, and (ii)  
756 the local thickness of superimposed ice, its internal drainage and  
757 meltwater refreezing. Such controlling factors maintain a down-glacier  
758 oriented topography throughout OSP1, whilst accommodating the  
759 declining roughness and anisotropy.



760  
761 **Figure 10:** Images of the observation plot on (A) July 31, DOY212, and  
762 (B) Aug 21, DOY233 that reveal the down-glacier oriented foliation and  
763 brighter ice dominates surface morphology during OSP1 while during  
764 OSP2, a more complex 'island' topography develops, reducing the  
765 dominance of the down-glacier orientation of relative relief.

766 In contrast, OSP2 showed a differing semivariogram form, with a  
767 dampened or absent cyclicity in the cross-glacier direction and, in the  
768 down-glacier direction, either an apparent sill at lag distances  $> 0.8$  m or  
769 tentative suggestions of cyclicity on the residual snow affected days.  
770 These semivariogram forms are suggestive of regular or irregular lenses  
771 or 'islands' on the surface (Pyrch and Deutsch, 2003). Here, the  
772 semivariograms were interpreted to indicate the surface topography  
773 evolved from structurally-controlled ridges in OSP1 to upstanding islands

774 0.4 m to 0.8 m long in the down-glacier direction and 0.5 m in the cross-  
775 glacier direction in OSP2 (Figure 10B). However, these islands appeared  
776 to be quasi-transient, decaying as residual snow melted and OSP2  
777 progressed further. While turbulent energy comprised a higher proportion  
778 of the total melt energy during this phase, ablation was less governed by  
779 albedo and likely more spatially uniform, but with melt rates remaining  
780 low, the ablating glacier ice likely experienced development of distributed  
781 rills and micro-channels, which progressively migrated over the surface  
782 (Rippin *et al.*, 2015; Mantelli *et al.*, 2015; Bash and Moorman, 2018).  
783 Such rills would be conducive to the formation of the transient ice islands;  
784 as ablation continues, these rills are subject to increasing meltwater  
785 fluxes, and establish a slope- or structure-defined drainage network  
786 thereby increasing surface roughness.

787 The evolutionary sequence we illustrate above (Figure 3B-3D) accords  
788 with the typical hydrological activation of an ablating glacier surface  
789 (Hambrey, 1977): sheetwash occurs on newly exposed ice with a portion  
790 refreezing, and as melting proceeds, meltwater flow initiates rills. As  
791 meltwater fluxes rise, this incipient drainage network then incises and  
792 develops. The maturing network is commonly influenced by surface slope  
793 and/or ice structure and becomes the antecedent topography for the  
794 following summer season. At Lower Foxfonna, during OSP2, the low rate  
795 of ablation reduces the hydrologically-driven amplification of roughness  
796 generated through the establishment of a drainage network. This reduced  
797 development of surface topography is exacerbated by several intertwined  
798 factors: Foxfonna's dominantly cold thermal regime, which reduces the  
799 energy available for melt and to change topography through ablation; the  
800 relative balance between radiative fluxes that promote the formation of  
801 roughness elements; and the turbulent fluxes that, by acting on the  
802 topographic highs, can reduce roughness. Consequently, the ice surface  
803 remains defined by small scale rills, and a general decrease in anisotropy  
804 towards zero, despite an increase in both the directional  $z_0$  metrics.

805 On the basis of our findings, we argue that the hydrology-roughness  
806 correlation, identified at a coarse scale by Rippin *et al.* (2015), may take  
807 two forms: firstly, down-glacier oriented topography aligned with  
808 structure and/or peak melt season hydrology; and secondly, topography  
809 generated by supraglacial rills that braid or anastomose. We hypothesise  
810 that the latter may be more common during cloudy periods with elevated  
811 turbulent energy fluxes, at least in cool Arctic summer conditions. Our  
812 dataset, owing to its brief duration and short singular synoptic time  
813 periods, did not allow us to robustly examine the role of turbulent energy  
814 fluxes in smoothing the glacier surface, as hypothesised by Muller and

815 Keeler (1969). It remains unclear, therefore, whether during periods  
816 dominated by turbulent energy flux, a feedback exists wherein continued  
817 braiding of rills an associate ice ablation supresses the evolution of  
818 roughness, or whether the meltwater volumes produced enable rill  
819 coalescence, incision and the evolution of a rougher surface.

#### 820 **4.4 Summary and wider relevance**

821 We highlight that traditional morphometric measures (e.g., Gallant and  
822 Wilson, 2000) at fine-resolution are ineffective in providing insight into  
823 bare-ice topographic variability, in part owing to the comparatively  
824 smooth nature of ablating glacier ice in the absence of lager scale  
825 roughness features (e.g., Cathles *et al.*, 2010; Dachauer *et al.*, 2021).  
826 However, at the 25 mm kernel-scale our data revealed an inverse  
827 association between blue-band surface brightness and Riley's roughness  
828 index. With knowledge that the Bearing Area Curves and z-score  
829 histograms revealed a near-surface variability and the blue-band albedo  
830 proxy offers a first-order discrimination between ice and impurities  
831 (Irvine-Fynn *et al.*, 2010), the relationship invoked the melting in and out  
832 of impurities, respectively increasing and decreasing albedo (e.g., Bøggild  
833 *et al.*, 2010). Lower albedo impurities may also include meltwater, or the  
834 water column that exists within features such as cryoconite holes (e.g.,  
835 Gribbon, 1979; Cook *et al.*, 2016; Takeuchi *et al.*, 2018). Consequently, it  
836 is important to note that the retrieval of ice surface topographic  
837 roughness metrics using photogrammetric techniques, including  
838 derivation of  $z_0$  estimates, may require consideration of refraction  
839 through-water. However, given the scale of features such as cryoconite  
840 holes and rills, such adjustments are most likely to have a small effect  
841 (Woodget *et al.*, 2015). In energy transfer terms, the aerodynamic  
842 roughness length may, locally, be defined by the water surface, not the  
843 ice surface; therefore, in areas exhibiting a high frequency of rills or  
844 water-filled topographic lows, spatial or temporal variations in the near-  
845 surface or surface water table (Cook *et al.*, 2016) may be an important  
846 consideration for defining seasonal and sub-seasonal patterns in  $z_0$ .  
847 Further evidence of hydrological controls on bare-ice roughness was found  
848 in the temporal evolution of the plot's profile-based and two-dimensional  
849 roughness metrics. This evolution followed Smith *et al.*'s (2020)  
850 conceptual model, and highlighted that the degradation of superimposed  
851 ice results in the rapid decline in  $z_0$  following the elimination of seasonal  
852 snow, while subsequent melt promotes a subtle increase in roughness.  
853 The analysis of semivariograms revealed the superimposed ice phase  
854 exhibits topography defined by antecedent, slope- and/or structure-

855 oriented features likely exploited by the hydrological activation of the  
856 surface. The presence or absence of superimposed ice may condition the  
857 magnitude, rate and duration of this initial bare-ice roughness decline.  
858 Then, as melt continues, and particularly under conditions of elevated  
859 turbulent energy fluxes, the bare-ice surface topography becomes  
860 characterised by the formation of braided rills and their development  
861 towards a parallel drainage network. It is unclear whether roughness  
862 stimulates rill geometry (e.g., Mantelli *et al.*, 2015) or ice structure and  
863 hydrology define the spatial arrangement of roughness. With the specific  
864 form of topography critical to the frontal area exposed to the prevailing  
865 wind, transitions between aligned and braided forms influence the true  
866 aerodynamic roughness lengths,  $z_0$ , and emphasise the need to employ  $z_{0S}$   
867 (Smith *et al.*, 2016) to characterise the surface metric. However, as  
868 this study reports a single site over a single melt season, separation of  
869 the coupled meteorological, ice structural and hydrological drivers  
870 remains equivocal and invites further study.

871 With evidence of hydrological controls underlying surface roughness,  
872 themselves associated with relative balances between radiative and  
873 turbulent energy drive ablation, we suggest the activation and evolution  
874 of supraglacial hydrology represents a primary control on bare-ice  $z_0$ .  
875 Variation in ablation regime and meltwater fluxes impacting on  $z_0$  can  
876 explain the contrasting, unsystematic or indiscriminate trajectories of  
877 roughness either over time particularly at the plot-scale (e.g., Brock *et al.*,  
878 2006; Guo *et al.*, 2018; Smith *et al.*, 2020; Lui *et al.*, 2020). Under  
879 melt regimes with higher turbulent energy fluxes, the maintenance of  
880 braided rills and micro-channels may suppress  $z_0$ . Consequently, we  
881 suggest that in a warming climate, in both Arctic and Alpine settings,  
882 owing to potential changes in the ratios between turbulent and radiative  
883 energy fluxes: (i) the ablation-to-accumulation season transition may  
884 experience reductions in  $z_0$ , and (ii) the hydrological response of glacier  
885 surfaces will define their aerodynamic roughness trajectory, surface  
886 anisotropy, and the morphology inherited from one year to the next.  
887 The advent of consumer-grade high-resolution imaging platforms,  
888 including uncrewed aerial vehicles, and photogrammetric software  
889 packages (e.g., Rippin *et al.*, 2015; Ryan *et al.*, 2015, 2017; Moorman  
890 and Bash, 2018) offers considerable opportunity to develop fine-scale  
891 bare-ice topographic time-series across multiple sites and years. Such  
892 data sets, and the analytical framework presented here, would facilitate  
893 (i) a refinement of the model of seasonal progression of surface  
894 roughness (Smith *et al.*, 2020), including end-of-melt-season trajectories;  
895 (ii) an improved understanding of the relative significance of the energy

896 balance components, ice structure, and rills or micro-channels in defining  
897 surface topography; and, (iii) better constraints on the retrieval of  
898 coarser-resolution satellite-derived measures, their variability and  
899 physical meaning. These are critical questions for improving projections of  
900 future glacier mass balance and seasonal runoff patterns in the Arctic and  
901 elsewhere, where snowlines are forecast to rise (e.g., Huss and Hock,  
902 2015; Ryan *et al.*, 2019; Noel *et al.*, 2019, 2020; Zebre *et al.*, 2021) and  
903 bare-ice extents and turbulent energy exchanges to increase, transiently  
904 on receding valley glaciers or more progressively around the margins of  
905 Greenland and Antarctica over the coming decades.

## 906 **5. CONCLUSIONS**

907 Modelling studies have forecast an increase in the extent of bare glacier  
908 ice during the summer melt season in the Arctic over the next few  
909 decades as air temperatures rise. The warmer air can contribute to raising  
910 ice ablation as turbulent energy fluxes increase, which themselves are  
911 modulated by the ice surface topography and its aerodynamic roughness.  
912 Employing a novel time-lapse digital imaging and photogrammetry  
913 methodology at a High-Arctic site, we demonstrate fine-scale temporal  
914 evolution of ice topography over two 9-day melt-season periods. Our data  
915 showed that traditional kernel-based geomorphological metrics commonly  
916 used to describe roughness were not effective in revealing the temporal  
917 dynamics in ice surface topography that were evident in profile-based and  
918 2-dimensional metrics. The anisotropic ice surface evidenced a  
919 progressive decline followed by an increase in aerodynamic roughness at  
920 the millimetre scale. Using a geostatistical and spectral analysis of the  
921 surface topography we demonstrate that roughness variations relate to  
922 the vertical movement of impurities and hydrological activation of the ice  
923 surface. Over time, down-glacier oriented, superimposed ice ridges  
924 transitioned to a bare-ice surface characterised by braiding rills, which  
925 highlights the importance of supraglacial hydrology in modulating surface  
926 roughness. With forecasts of rising air temperatures, cloudiness and  
927 rainfall in Arctic latitudes, augmented turbulent energy fluxes may result  
928 in the increased prevalence of rill-dominated hydrology. Consequently, to  
929 better constrain seasonal and sub-seasonal trajectories of glacier  
930 topography to employ within numerical mass balance models, we suggest  
931 our analytical approach provides a framework for future studies using  
932 fine-scale digital surface models. Assessments should exploit not only  
933 topographic time-series, but also integrate geostatistical analyses coupled  
934 with meteorological data to identify both time-variable process and form.  
935

936 **REFERENCES**

- 937 Allmaras, R. R., Burwell, R. E., Larson, W. E., & Holt, R. F. (1966). Total  
938 porosity and random roughness of the interrow zone as influenced by  
939 tillage. USDA Conservation Research Report, 7, 22 pp.
- 940 Arnold, N. S., Rees, W. G., Hodson, A. J., & Kohler, J. (2006).  
941 Topographic controls on the surface energy balance of a high Arctic valley  
942 glacier. *Journal of Geophysical Research: Earth Surface*, **111**(F2).
- 943 Ascione, A., Cinque, A., Miccadei, E., Villani, F. and Berti, C. (2008). The  
944 Plio-Quaternary uplift of the Apennine chain: new data from the analysis  
945 of topography and river valleys in Central Italy. *Geomorphology*, **102**(1),  
946 105-118.
- 947 Bash, E. A., & Moorman, B. J. (2020). Surface melt and the importance of  
948 water flow – an analysis based on high-resolution unmanned aerial  
949 vehicle (UAV) data for an Arctic glacier. *The Cryosphere*, **14**(2), 549-563.
- 950 Bintanja, R. (2018). The impact of Arctic warming on increased rainfall.  
951 *Scientific Reports*, **8**(1), 1-6.
- 952 Bintanja, R., van der Wiel, K., Van der Linden, E. C., Reusen, J., Bogerd,  
953 L., Krikken, F., & Selten, F. M. (2020). Strong future increases in Arctic  
954 precipitation variability linked to poleward moisture transport. *Science*  
955 *Advances*, **6**(7), eaax6869.
- 956 Bøggild, C. E., Brandt, R. E., Brown, K. J., & Warren, S. G. (2010). The  
957 ablation zone in northeast Greenland: ice types, albedos and impurities.  
958 *Journal of Glaciology*, **56**(195), 101-113.
- 959 Brasington, J., Vericat, D., & Rychkov, I. (2012). Modeling river bed  
960 morphology, roughness, and surface sedimentology using high resolution  
961 terrestrial laser scanning. *Water Resources Research*, **48**(11), W11519.
- 962 Brock, B. W., & Arnold, N. S. (2000). A spreadsheet-based (Microsoft  
963 Excel) point surface energy balance model for glacier and snow melt  
964 studies. *Earth Surface Processes and Landforms*, **25**(6), 649-658.
- 965 Brock, B. W., Willis, I. C., Sharp, M. J., & Arnold, N. S. (2000). Modelling  
966 seasonal and spatial variations in the surface energy balance of Haut  
967 Glacier d’Arolla, Switzerland. *Annals of Glaciology*, **31**, 53-62.
- 968 Brock, B. W., Willis, I. C., & Sharp, M. J. (2006). Measurement and  
969 parameterization of aerodynamic roughness length variations at Haut  
970 Glacier d’Arolla, Switzerland. *Journal of Glaciology*, **52**(177), 281-297.
- 971 Cathles, L. M., Abbot, D. S., Bassis, J. N., & MacAyeal, D. R. (2011).  
972 Modeling surface-roughness/solar-ablation feedback: application to small-

- 973 scale surface channels and crevasses of the Greenland ice sheet. *Annals*  
974 *of Glaciology*, **52**(59), 99-108.
- 975 Chambers, J. R., Smith, M. W., Quincey, D. J., Carrivick, J. L., Ross, A.  
976 N., & James, M. R. (2020). Glacial Aerodynamic roughness estimates:  
977 uncertainty, sensitivity, and precision in field measurements. *Journal of*  
978 *Geophysical Research: Earth Surface*, **125**(2), e2019JF005167.
- 979 Chambers, J.R., Smith, M.W., Smith, T., Sailer, R., Quincey, D.J.,  
980 Carrivick, J.L., Nicholson, L., Mertes, J., Stiperski, I. and James, M.R.,  
981 2021. Correcting for systematic underestimation of topographic glacier  
982 aerodynamic roughness values from Hintereisferner, Austria. *Frontiers in*  
983 *Earth Science*, **9**, 435.
- 984 Chandler, D. M., Alcock, J. D., Wadham, J. L., Mackie, S. L., & Telling, J.  
985 (2015). Seasonal changes of ice surface characteristics and productivity in  
986 the ablation zone of the Greenland Ice Sheet. *The Cryosphere*, **9**(2), 487-  
987 504.
- 988 Christiansen, H. H., French, H. M., & Humlum, O. (2005). Permafrost in  
989 the Gruve-7 mine, Adventdalen, Svalbard. *Norsk Geografisk Tidsskrift*,  
990 **59**(2), 109-115.
- 991 Cook, J. M., Hodson, A. J., & Irvine-Fynn, T. D. (2016). Supraglacial  
992 weathering crust dynamics inferred from cryoconite hole hydrology.  
993 *Hydrological Processes*, **30**(3), 433-446.
- 994 Conway, J. P., & Cullen, N. J. (2013). Constraining turbulent heat flux  
995 parameterization over a temperate maritime glacier in New Zealand.  
996 *Annals of Glaciology*, **54**(63), 41-51.
- 997 Cuffey, K. M., & Paterson, W. S. B. (2010). *The physics of glaciers*.  
998 Academic Press.
- 999 Curley, A. N., Kochtitzky, W. H., Edwards, B. R., & Copland, L. (2021).  
1000 Glacier changes over the past 144 years at Alexandra Fiord, Ellesmere  
1001 Island, Canada. *Journal of Glaciology*, **67**(263), 511-522.
- 1002 Currence, H.D., Lovely, W.G. (1970). The analysis of soil surface  
1003 roughness. *Transactions of the ASAE*, **13**(6), 710-714.
- 1004 Dachauer, A., Hann, R., & Hodson, A. J. (2021). Aerodynamic roughness  
1005 length of crevassed tidewater glaciers from UAV mapping. *The*  
1006 *Cryosphere*, **15**, 5513-5528.
- 1007 Doyle, S.H., Hubbard, A., van De Wal, R.S., Box, J.E., van As, D.,  
1008 Scharrer, K., Meierbachtol, T.W., Smeets, P.C., Harper, J.T., Johansson,  
1009 E. and Mottram, R.H., 2015. Amplified melt and flow of the Greenland ice



- 1010 sheet driven by late-summer cyclonic rainfall. *Nature Geoscience*, **8**(8),  
1011 647-653.
- 1012 Fausto, R. S., van As, D., Box, J. E., Colgan, W., Langen, P. L., &  
1013 Mottram, R. H. (2016). The implication of nonradiative energy fluxes  
1014 dominating Greenland ice sheet exceptional ablation area surface melt in  
1015 2012. *Geophysical Research Letters*, **43**(6), 2649-2658.
- 1016 Fitzpatrick, N., Radić, V., & Menounos, B. (2019). A multi-season  
1017 investigation of glacier surface roughness lengths through in situ and  
1018 remote observation. *The Cryosphere*, **13**(3), 1051-1071.
- 1019 Giesen, R. H., Andreassen, L. M., Oerlemans, J., & Van Den Broeke, M. R.  
1020 (2014). Surface energy balance in the ablation zone of Langfjordjøkelen,  
1021 an Arctic, maritime glacier in northern Norway. *Journal of Glaciology*,  
1022 **60**(219), 57-70.
- 1023 Gillett, S., & Cullen, N. J. (2011). Atmospheric controls on summer  
1024 ablation over Brewster Glacier, New Zealand. *International Journal of*  
1025 *Climatology*, **31**(13), 2033-2048.
- 1026 Greuell, W., & de Wildt, M. D. R. (1999). Anisotropic reflection by melting  
1027 glacier ice: measurements and parametrizations in Landsat TM bands 2  
1028 and 4. *Remote Sensing of Environment*, **70**(3), 265-277.
- 1029 Gribbon, P. W. F. (1979). Cryoconite holes on Sermikavsak, west  
1030 Greenland. *Journal of Glaciology*, **22**(86), 177-181.
- 1031 Guo, X., Yang, K., Zhao, L., Yang, W., Li, S., Zhu, M., Yao, T. and Chen,  
1032 Y., 2011. Critical evaluation of scalar roughness length parametrizations  
1033 over a melting valley glacier. *Boundary-layer Meteorology*, **139**(2), 307-  
1034 332.
- 1035 Guo, S., Chen, R., Liu, G., Han, C., Song, Y., Liu, J., Yang, Y., Liu, Z.,  
1036 Wang, X., Liu, X. and Wang, L., 2018. Simple parameterization of  
1037 aerodynamic roughness lengths and the turbulent heat fluxes at the top  
1038 of midlatitude August-One Glacier, Qilian Mountains, China. *Journal of*  
1039 *Geophysical Research: Atmospheres*, **123**(21), 12-066.
- 1040 Hambrey, M. J. (1977). Supraglacial drainage and its relationship to  
1041 structure, with particular reference to Charles Rabots Bre, Okstindan,  
1042 Norway. *Norsk Geografiska Tidsskrift*, **31**, 69-77
- 1043 Hambrey, M. J., & Lawson, W. (2000). Structural styles and deformation  
1044 fields in glaciers: a review. *Geological Society Special Publications*,  
1045 **176**(1), 59-83.

- 1046 Hanssen-Bauer, I., Førland, E. J., Hisdal, H., Mayer, S., Sandø, A. B., &  
1047 Sorteberg, A. (2019). Climate in Svalbard 2100. A knowledge base for  
1048 climate adaptation.
- 1049 Hanssen-Bauer, I., Kristensen Solås, M., and Steffensen, E. L. (1990).  
1050 The climate of Spitsbergen. Klima Report Series of the Norwegian  
1051 Meteorological Institute, 39/90, pp.40.
- 1052 Hay, J. E., & Fitzharris, B. B. (1988). A comparison of the energy-balance  
1053 and bulk-aerodynamic approaches for estimating glacier melt. *Journal of*  
1054 *Glaciology*, **34**(117), 145-153.
- 1055 Herzfeld, U. C., Box, J. E., Steffen, K., Mayer, H., Caine, N., & Losleben,  
1056 M. V. (2003). A case study on the influence of snow and ice surface  
1057 roughness on melt energy. *Zeitschrift für Gletscherkunde und*  
1058 *Glazialgeologie*, **39**, 1-42.
- 1059 Herzfeld, U. C., Mayer, H., Feller, W., & Mimler, M. (2000). Geostatistical  
1060 analysis of glacier-roughness data. *Annals of Glaciology*, **30**, 235-242.
- 1061 Hock, R. (2005). Glacier melt: a review of processes and their modelling.  
1062 *Progress in Physical Geography*, **29**(3), 362-391.
- 1063 Hudleston, P. J. (2015). Structures and fabrics in glacial ice: A review.  
1064 *Journal of Structural Geology*, **81**, 1-27.
- 1065 Huss, M., & Hock, R. (2015). A new model for global glacier change and  
1066 sea-level rise. *Frontiers in Earth Science*, **3**, 54.
- 1067 Irvine-Fynn, T. D., Bridge, J. W., & Hodson, A. J. (2010). Rapid  
1068 quantification of cryoconite: granule geometry and in situ supraglacial  
1069 extents, using examples from Svalbard and Greenland. *Journal of*  
1070 *Glaciology*, **56**(196), 297-308.
- 1071 Irvine-Fynn, T. D., Bridge, J. W., & Hodson, A. J. (2011). In situ  
1072 quantification of supraglacial cryoconite morphodynamics using time-  
1073 lapse imaging: an example from Svalbard. *Journal of Glaciology*, **57**(204),  
1074 651-657.
- 1075 Irvine-Fynn, T. D., Hanna, E., Barrand, N. E., Porter, P. R., Kohler, J., &  
1076 Hodson, A. J. (2014b). Examination of a physically based, high-resolution,  
1077 distributed Arctic temperature-index melt model, on Midtre Lovénbreen,  
1078 Svalbard. *Hydrological Processes*, **28**(1), 134-149.
- 1079 Irvine-Fynn, T. D., Sanz-Ablanedo, E., Rutter, N., Smith, M. W., &  
1080 Chandler, J. H. (2014a). Measuring glacier surface roughness using plot-  
1081 scale, close-range digital photogrammetry. *Journal of Glaciology*,  
1082 **60**(223), 957-969.

- 1083 James, T. D., Carbonneau, P. E., & Lane, S. N. (2007). Investigating the  
1084 effects of DEM error in scaling analysis. *Photogrammetric Engineering &*  
1085 *Remote Sensing*, **73**(1), 67-78.
- 1086 Jenness, J. (2006). Topographic Position Index (tpi\_jen.avx) extension for  
1087 ArcView 3.x, v. 1.3a. Jenness Enterprises. Available at:  
1088 <http://www.jennessent.com/arcview/tpi.htm>.
- 1089 Jennings, S. J. A., & Hambrey, M. J. (2021). Structures and deformation  
1090 in glaciers and ice sheets. *Reviews of Geophysics*, **59**, e2021RG000743.
- 1091 Journel A. G. and Huijbregts, C. J. (1978). Mining Geostatistics. Academic  
1092 Press, New York.
- 1093 Koziol, K. A., Moggridge, H. L., Cook, J. M., & Hodson, A. J. (2019).  
1094 Organic carbon fluxes of a glacier surface: A case study of Foxfonna, a  
1095 small Arctic glacier. *Earth Surface Processes and Landforms*, **44**(2), 405-  
1096 416.
- 1097 Liestøl, O. 1974. Glaciological work in 1972. *Norsk Polarinstitutt Årbok*,  
1098 125-135.
- 1099 Lindsay, J. B., Cockburn, J. M. H., & Russell, H. A. J. (2015). An integral  
1100 image approach to performing multi-scale topographic position analysis.  
1101 *Geomorphology*, **245**, 51-61.
- 1102 Lindsay, J. B., Newman, D. R., & Francioni, A. (2019). Scale-optimized  
1103 surface roughness for topographic analysis. *Geosciences*, **9**(7), 322.
- 1104 Liu, J., Chen, R., & Han, C. (2020). Spatial and temporal variations in  
1105 glacier aerodynamic surface roughness during the melting season, as  
1106 estimated at the August-One ice cap, Qilian mountains, China. *The*  
1107 *Cryosphere*, **14**(3), 967-984.
- 1108 Mantelli, E., Camporeale, C., & Ridolfi, L. (2015). Supraglacial channel  
1109 inception: Modeling and processes. *Water Resources Research*, **51**(9),  
1110 7044-7063.
- 1111 Martín-Español, A., Navarro, F. J., Otero, J., Lapazaran, J. J., & Błaszczyk,  
1112 M. (2015). Estimate of the total volume of Svalbard glaciers, and their  
1113 potential contribution to sea-level rise, using new regionally based scaling  
1114 relationships. *Journal of Glaciology*, **61**(225), 29-41.
- 1115 Middlemas, E. A., Kay, J. E., Medeiros, B. M., & Maroon, E. A. (2020).  
1116 Quantifying the influence of cloud radiative feedbacks on Arctic surface  
1117 warming using cloud locking in an Earth system model. *Geophysical*  
1118 *Research Letters*, **47**(15), e2020GL089207.

- 1119 Mulla, D. J. (1988). Using geostatistics and spectral analysis to study  
 1120 spatial patterns in the topography of southeastern Washington State,  
 1121 USA. *Earth Surface Processes and Landforms*, **13**(5), 389-405.
- 1122 Müller, F., & Keeler, C. M. (1969). Errors in short-term ablation  
 1123 measurements on melting ice surfaces. *Journal of Glaciology*, **8**(52), 91-  
 1124 105.
- 1125 Munro, D. S. (1989). Surface roughness and bulk heat transfer on a  
 1126 glacier: comparison with eddy correlation. *Journal of Glaciology*, **35**(121),  
 1127 343-348.
- 1128 Nield, J. M., Chiverrell, R. C., Darby, S. E., Leyland, J., Vircavs, L. H., &  
 1129 Jacobs, B. (2013). Complex spatial feedbacks of tephra redistribution, ice  
 1130 melt and surface roughness modulate ablation on tephra covered glaciers.  
 1131 *Earth Surface Processes and Landforms*, **38**(1), 95-102.
- 1132 Noël, B., van de Berg, W. J., Lhermitte, S., & van den Broeke, M. R.  
 1133 (2019). Rapid ablation zone expansion amplifies north Greenland mass  
 1134 loss. *Science Advances*, **5**(9), eaaw0123.
- 1135 Noël, B., Jakobs, C.L., van Pelt, W.J.J., Lhermitte, S., Wouters, B., Kohler,  
 1136 J., Hagen, J.O., Luks, B., Reijmer, C.H., van de Berg, W.J. and van den  
 1137 Broeke, M.R., 2020. Low elevation of Svalbard glaciers drives high mass  
 1138 loss variability. *Nature Communications*, **11**(1), 1-8.
- 1139 Østby, T. I., Schuler, T. V., Hagen, J. O., Hock, R., Kohler, J., & Reijmer,  
 1140 C. H. (2017). Diagnosing the decline in climatic mass balance of glaciers  
 1141 in Svalbard over 1957–2014. *The Cryosphere*, **11**(1), 191-215.
- 1142 Overland, J., Dunlea, E., Box, J.E., Corell, R., Forsius, M., Kattsov, V.,  
 1143 Olsen, M.S., Pawlak, J., Reiersen, L.O. and Wang, M., 2019. The urgency  
 1144 of Arctic change. *Polar Science*, **21**, 6-13.
- 1145 Perron, J. T., Kirchner, J. W., & Dietrich, W. E. (2008). Spectral  
 1146 signatures of characteristic spatial scales and nonfractal structure in  
 1147 landscapes. *Journal of Geophysical Research: Earth Surface*, **113**(F4),  
 1148 F04003.
- 1149 Pyrcz, M.J. and Deutsch, C.V., 2003. The whole story on the hole effect.  
 1150 *Geostatistical Association of Australasia Newsletter*, **18**, 3-5
- 1151 Rees, W. G., & Arnold, N. S. (2006). Scale-dependent roughness of a  
 1152 glacier surface: implications for radar backscatter and aerodynamic  
 1153 roughness modelling. *Journal of Glaciology*, **52**(177), 214-222.
- 1154 Riley, S.J., DeGloria, S.D. and Elliot, R., 1999. Index that quantifies  
 1155 topographic heterogeneity. *Intermountain Journal of Sciences*, **5**(1-4),  
 1156 23-27.

- 1157 Rippin, D. M., Pomfret, A., & King, N. (2015). High resolution mapping of  
 1158 supra-glacial drainage pathways reveals link between micro-channel  
 1159 drainage density, surface roughness and surface reflectance. *Earth*  
 1160 *Surface Processes and Landforms*, **40**(10), 1279-1290.
- 1161 Romkens, M. J., & Wang, J. Y. (1986). Effect of tillage on surface  
 1162 roughness. *Transactions of the ASAE*, **29**(2), 429-0433.
- 1163 Rossini, M., Di Mauro, B., Garzonio, R., Baccolo, G., Cavallini, G.,  
 1164 Mattavelli, M., De Amicis, M. and Colombo, R., 2018. Rapid melting  
 1165 dynamics of an alpine glacier with repeated UAV photogrammetry.  
 1166 *Geomorphology*, **304**, 159-172.
- 1167 Rutter, N., Hodson, A., Irvine-Fynn, T., & Solås, M. K. (2011). Hydrology  
 1168 and hydrochemistry of a deglaciating high-Arctic catchment, Svalbard.  
 1169 *Journal of Hydrology*, **410**(1-2), 39-50.
- 1170 Ryan, J.C., Hubbard, A., Box, J.E., Brough, S., Cameron, K., Cook, J.M.,  
 1171 Cooper, M., Doyle, S.H., Edwards, A., Holt, T. and Irvine-Fynn, T., 2017.  
 1172 Derivation of high spatial resolution albedo from UAV digital imagery:  
 1173 application over the Greenland Ice Sheet. *Frontiers in Earth Science*, **5**,  
 1174 40.
- 1175 Ryan, J. C., Hubbard, A., Irvine-Fynn, T. D., Doyle, S. H., Cook, J. M.,  
 1176 Stibal, M., & Box, J. E. (2017). How robust are in situ observations for  
 1177 validating satellite-derived albedo over the dark zone of the Greenland Ice  
 1178 Sheet?. *Geophysical Research Letters*, **44**(12), 6218-6225.
- 1179 Ryan, J. C., Smith, L. C., Van As, D., Cooley, S. W., Cooper, M. G.,  
 1180 Pitcher, L. H., & Hubbard, A. (2019). Greenland Ice Sheet surface melt  
 1181 amplified by snowline migration and bare ice exposure. *Science Advances*,  
 1182 **5**(3), eaav3738.
- 1183 Schneider, C.A., Rasband, W.S., Eliceiri, K.W. (2012). NIH Image to  
 1184 ImageJ: 25 years of image analysis. *Nature Methods*, **9**, 671-675.
- 1185 Smeets, C. J. P. P., Duynkerke, P. G., & Vugts, H. F. (1999). Observed  
 1186 wind profiles and turbulence fluxes over an ice surface with changing  
 1187 surface roughness. *Boundary-Layer Meteorology*, **92**(1), 99-121.
- 1188 Smeets, C. J. P. P., van den Broeke, M. R. (2008). Temporal and spatial  
 1189 variations of the aerodynamic roughness length in the ablation zone of  
 1190 the Greenland ice sheet. *Boundary-layer Meteorology*, **128**(3), 315-338.
- 1191 Smith, B. E., Raymond, C. F., Scambos, T. (2006). Anisotropic texture of  
 1192 ice sheet surfaces. *Journal of Geophysical Research: Earth Surface*,  
 1193 **111**(F1).

- 1194 Smith, M.W. (2014). Roughness in the earth sciences. *Earth-Science*  
1195 *Reviews*, **136**, 202-225.
- 1196 Smith, M. W., Quincey, D. J., Dixon, T., Bingham, R. G., Carrivick, J. L.,  
1197 Irvine-Fynn, T. D., & Rippin, D. M. (2016). Aerodynamic roughness of  
1198 glacial ice surfaces derived from high-resolution topographic data. *Journal*  
1199 *of Geophysical Research: Earth Surface*, **121**(4), 748-766.
- 1200 Smith, T., Smith, M.W., Chambers, J.R., Sailer, R., Nicholson, L., Mertes,  
1201 J., Quincey, D.J., Carrivick, J.L. and Stiperski, I. (2020). A scale-  
1202 dependent model to represent changing aerodynamic roughness of  
1203 ablating glacier ice based on repeat topographic surveys. *Journal of*  
1204 *Glaciology*, **66**(260), 950-964.
- 1205 Smith, M. W., Vericat, D. (2015). From experimental plots to  
1206 experimental landscapes: topography, erosion and deposition in sub-  
1207 humid badlands from structure-from-motion photogrammetry. *Earth*  
1208 *Surface Processes and Landforms*, **40**(12), 1656-1671.
- 1209 Spagnolo, M., Bartholomaus, T.C., Clark, C.D., Stokes, C.R., Atkinson, N.,  
1210 Dowdeswell, J.A., Ely, J.C., Graham, A.G., Hogan, K.A., King, E.C. and  
1211 Larter, R.D. (2017). The periodic topography of ice stream beds: Insights  
1212 from the Fourier spectra of mega-scale glacial lineations. *Journal of*  
1213 *Geophysical Research: Earth Surface*, **122**(7), 1355-1373.
- 1214 Takeuchi, N., Sakaki, R., Uetake, J., Nagatsuka, N., Shimada, R., Niwano,  
1215 M., Aoki, T. (2018). Temporal variations of cryoconite holes and  
1216 cryoconite coverage on the ablation ice surface of Qaanaaq Glacier in  
1217 northwest Greenland. *Annals of Glaciology*, **59**(77), 21-30.
- 1218 Telling, J., Anesio, A.M., Tranter, M., Stibal, M., Hawkings, J., Irvine-Fynn,  
1219 T., Hodson, A., Butler, C., Yallop, M. and Wadham, J. (2012). Controls on  
1220 the autochthonous production and respiration of organic matter in  
1221 cryoconite holes on high Arctic glaciers. *Journal of Geophysical Research:*  
1222 *Biogeosciences*, **117**(G1), G01017.
- 1223 van den Broeke, M., Box, J., Fettweis, X., Hanna, E., Noël, B., Tedesco,  
1224 M., van As, D., van de Berg, W.J., van Kampenhout, L. (2017). Greenland  
1225 ice sheet surface mass loss: recent developments in observation and  
1226 modeling. *Current Climate Change Reports*, **3**(4), 345-356.
- 1227 van Tiggelen, M., Smeets, P.C., Reijmer, C.H., Wouters, B., Steiner, J.F.,  
1228 Nieuwstraten, E.J., Immerzeel, W.W., van den Broeke, M.R. (2021).  
1229 Mapping the aerodynamic roughness of the Greenland ice sheet surface  
1230 using ICESat-2: Evaluation over the K-transect. *The Cryosphere*, **15**(6),  
1231 2601-2621.

- 1232 Wackrow, R., Chandler, J.H. (2008). A convergent image configuration for  
1233 DEM extraction that minimises the systematic effects caused by an  
1234 inaccurate lens model. *Photogrammetric Record*, **23**(121): 6-18.
- 1235 Wadham, J. L., & Nuttall, A. M. (2002). Multiphase formation of  
1236 superimposed ice during a mass-balance year at a maritime high-Arctic  
1237 glacier. *Journal of Glaciology*, **48**(163), 545-551.
- 1238 Wilson, J. P., & Gallant, J. C. (Eds). (2000). Digital terrain analysis.  
1239 Terrain analysis: Principles and applications. John Wiley & Sons, New  
1240 York, 520 pp.
- 1241 Willis, I.C., Arnold, N.S., Brock, B.W. (2002). Effect of snowpack removal  
1242 on energy balance, melt and runoff in a small supraglacial catchment.  
1243 *Hydrological Processes*, **16**(14), 2721-2749.
- 1244 Woodget, A. S., Carbonneau, P. E., Visser, F., & Maddock, I. P. (2015).  
1245 Quantifying submerged fluvial topography using hyperspatial resolution  
1246 UAS imagery and structure from motion photogrammetry. *Earth Surface  
1247 Processes and Landforms*, **40**(1), 47-64.
- 1248 Wolf, P.R., Dewitt, B.A. (2000). Elements of Photogrammetry, with  
1249 Applications in GIS. McGraw-Hill, New York, 608 pp.
- 1250 Žebre, M., Colucci, R. R., Giorgi, F., Glasser, N. F., Racoviteanu, A. E., &  
1251 Del Gobbo, C. (2021). 200 years of equilibrium-line altitude variability  
1252 across the European Alps (1901– 2100). *Climate Dynamics*, **56**(3), 1183-  
1253 1201.  
1254  
1255